

# **Transmit coil for ultrawideband magnetic field generation**

**Kuba Jaloszynski**

**June, 2025**

**Master Thesis**





## **Transmit coil for ultrawideband magnetic field generation**

Master Thesis  
June, 2025

By  
Kuba Jaloszynski

Supervised by:  
Vitaliy Zhurbenko

Copyright: Reproduction of this publication in whole or in part must include the customary bibliographic citation, including author attribution, report title, etc.  
Cover photo: Vibeke Hempler, 2012  
Published by: DTU, Department of Space Research and Technology, Elektrovej, Building 327, 2800 Kgs. Lyngby Denmark

## **Approval**

This thesis has been prepared over five months at the Section for Electromagnetic systems, Department of Space Research and Technology, at the Technical University of Denmark, DTU, in partial fulfilment for the degree Master of Science in Engineering, MSc Eng.

It is assumed that the reader has a basic knowledge in the areas of electronics and physics of magnetic fields.

Kuba Jaloszynski - s232674

.....  
*Signature*

.....  
*Date*

## Abstract

Modern state of the art MRIs play a key role in medical diagnosis. These are relatively simple devices. To create an image they utilize the bursts of radio-frequency waves to temporarily disturb the magnetic polarity of atoms aligned by the primary static magnetic field. Conventional MRIs are tuned to a very specific frequency, usually corresponding to resonance frequency of hydrogen protons ( $\approx 127.7\text{ MHz}$ ). While this provides high-quality hydrogen images, there is no feasible way to change the tuning frequency for mapping other types of tissues. The primary obstacle to overcoming this limitation has been the availability of the materials that could replace the existing electronic system inside the device's RF emitter. With the recent emergence of gallium nitride as a core material for modern high-speed, high-power FET transistors has created a set of new possibilities to improve MRI technology. Using GaN FET it is possible to replace simple L-C oscillator circuit with a more sophisticated, broadband, frequency controllable alternative, that promises to make the MRI a more versatile device, enabling imaging of multiple nuclei. A detailed and baseline for a following thesis was presented in "*Any-nucleus distributed active programmable transmit coil*"[1] by Han et al. This paper takes the design of ADAPT coil one step further, verifying design assumptions, increasing its power output and optimizing for scalability. The first chapter 1 gives the reader the introduction to the Magnetic Resonance Imaging (MRI). It should provide the basis to understand how the image is created, what is required, but also, what are the current limitations of the MRI devices, RF coil currently used and give the starting point to how to overcome these limits with an ADAPT coil. Next, reader is transitioned to the next, chapter 2 focused on review of ADAPT, where it is presented in detail, how an ADAPT coil is designed compared to conventional coil, how field effect transistor can replace the tuning element of the circuit, what are the gains of using the ADAPT coil and why is it not an ideal solution yet. Before further analysis and improvement suggestions of the coil, chapter 3 should make the reader familiar with the critical FET characteristics, how emerge of Gallium Nitride (GaN), allowed to overcome some of the obstacles, what are the future perspectives and gives a short overview on the process of FET selection for improving ADAPT coil. In chapter 4 presented are results of the simulations for both reference coil circuit, with minor changes to increase the simulation accuracy and verification of magnetic field simulations, and for the improvement suggestion that should allow driving coil at higher power, what directly translates to improvement in MRI operation. The chapter is summarized with the comparison of the simulated performance for reference and improved coils. Chapter 5 describes the PCB layout process, what are the exact changes made to the components list with expected impact of each of the elements and cost estimation for a proposed coil module. In chapter 6 described is the coil assembly with size corresponding to ADAPT coil, for direct performance comparison. Additionally, the whole body coil is given as a potential solution to increasing the imaging area done by the coil. Last chapter 7 contains the conclusions made after finishing the improvement of the ADAPT coil, thoughts on the next steps to be taken to test and improve the coil even further and the summary of this paper, and the summary of the paper.

## **Acknowledgements**

**Vitaliy Zhurbenko**, Associate Professor, DTU  
Supervisor

for unparalleled support and guidance during the thesis preparation.

**Mathias Hommelgaard**, PhD student, DTU

**Lisa Seidl**, PhD student, DTU

**Greta Giarola**, PhD student, DTU

thoughtful thesis review and help in creation of (BAM) concept.

**Christian Nicolai Nielsen**, MSc Civil Engineering, DTU

Creator of this thesis template.

# Contents

Approval . . . . .	ii
Abstract . . . . .	iii
Acknowledgements . . . . .	iv
<b>1 Introduction to MRI</b>	<b>1</b>
1.1 Fundamentals of Magnetic Resonance Imaging . . . . .	1
1.2 Conventional MRI limitations . . . . .	6
<b>2 ADAPT coil analysis</b>	<b>9</b>
2.1 ADAPT overview . . . . .	9
2.2 Advantages of ADAPT architecture . . . . .	11
2.3 Limitations of ADAPT coil . . . . .	12
2.4 Scope of ADAPT improvements - ADAPT module . . . . .	13
<b>3 FET technologies and drivers for high-power MRI systems</b>	<b>15</b>
3.1 FET selection criteria . . . . .	15
3.2 FET critical characteristics . . . . .	15
3.3 FET for MRI power electronics . . . . .	15
3.4 High performance driver devices . . . . .	18
3.5 Integrated and discrete drivers . . . . .	20
3.6 Device selection and validation . . . . .	20
<b>4 ADAPT Simulations</b>	<b>25</b>
4.1 ADAPT coil baseline circuit simulations . . . . .	25
4.2 Magneto-static simulations . . . . .	29
4.3 ADAPT coil module circuit simulations . . . . .	31
<b>5 ADAPT module layout</b>	<b>37</b>
5.1 ADAPT module layout overview . . . . .	37
5.2 Estimated cost of the ADAPT module . . . . .	41
<b>6 ADAPT module - assembly example</b>	<b>43</b>
6.1 9 cm diameter coil . . . . .	43
6.2 Full body coil . . . . .	44
<b>7 Summary and conclusions</b>	<b>47</b>
7.1 Summary . . . . .	48
<b>Bibliography</b>	<b>49</b>
<b>A ADAPT extension module schematic</b>	<b>51</b>
<b>List of Acronyms</b>	<b>53</b>



# 1 Introduction to MRI

Magnetic Resonance Imaging (MRI) since its introduction in the early 1980s has become an indispensable tool in medical diagnosis. Unlike X-ray based imaging, MRI is non-invasive way of generating high-resolution images of organs, tissues, detecting anomalies and characterizing conditions. The following chapter introduces principles of MRI technology and should give the basis for the discussion in further chapters of this paper.

## 1.1 Fundamentals of Magnetic Resonance Imaging

### 1.1.1 Hardware overview

A model MRI device is built with 4 main elements that enables image creation.

1. Primary magnet
2. Gradient coils
3. RF transmitter and receiver coils
4. User interface

#### Primary magnet

Generates high-intensity static magnetic field to polarize protons in a patient's body. Primary static field is denoted with  $B_0$  and has typical application value of 0.1T (low field) to 7T (high field). Devices with  $B_0 > 7\text{T}$  are primarily used for research; clinical diagnosis is rare due to practical constraints (size, cost, complexity, weight) these are limited to few research facilities. World strongest field operating MRI is the "Iseult" project [Fig:1.1] located at CEA-Paris-Saclay with 11.7T field intensity.

MRI is characterized by its field strength, with following general categories:

- $< 1\text{T}$  - Low field MRI, usually open bore
- $1\text{T}$  to  $1.5\text{T}$  - Mid field MRI
- $1.5\text{T}$  to  $7\text{T}$  - High and Very High field MRI
- $> 7\text{T}$  - Ultra High field MRI

According to several market reports and forecasts<sup>1,2,3,4</sup> global market is dominated by mid field (1.5T) MRIs with a market share estimated in range of 50% to 70%. In European market the majority of MRIs used are high field units (3T) with a market share of  $\approx 61\%$ .

The figure 1.2 shown the impact of MRI static field  $B_0$  on the image detail level.

#### Gradient coils

Large electrical conductors placed around main magnet bore. The main function of gradient coils is generation of a controlled magnetic field gradient applied to main  $B_0$  magnetic field, causing the magnetic field increase on one end and decrease on the other end. This allows focusing the imaging on a specific slice of tissue and spatial encoding.

---

<sup>1</sup>MRI system market

<sup>2</sup>A new era ushering in with 0.2T VLFS MRI 2

<sup>3</sup>Europe MRI Market

<sup>4</sup>MRI systems market size, share, and growth forecast from 2025-2032

## RF transmitter and receiver coils

Transmitter coil generates oscillating magnetic field ( $B_1$ ) to excite nuclei. The coil is tuned to Larmor frequency - resonant frequency of nuclei in the main magnetic field, and it is essential for image creation. Larmor frequency of nuclei can be estimated using formula [2]:

$$f_{larmor} = \gamma B_0 \quad (1.1)$$

where:

$f$  - Larmor frequency in Hertz

$\gamma$  - Gyromagnetic ratio ( $\frac{MHz}{T}$ )

$B_0$  - Magnetic field strength

For a typical 3T MRI tuned to  $^1H$  ( $\gamma = 42.58 \frac{MHz}{T}$ ) larmor frequency is:

$$f_{larmor} = 42.58 \frac{MHz}{T} \cdot 3T = 127.74 MHz$$

When excited, nuclei induce a current in the receiver coil, which is measured, amplified and processed to the final image.

Conventional coils are simple LC oscillator circuits tuned to the resonant (Larmor) frequency. The resonance frequency of a coil is given by:

$$f_0 = \frac{1}{2\pi\sqrt{LC}} \quad (1.2)$$

### Example matching for $^1H$

$$f_0 = f_{larmor}$$

then

$$C = \frac{1}{L \cdot (f_{larmor} \cdot 2 \cdot \pi)^2}$$

assuming  $L = 100 nH$

$$C = 15.55 pF$$

While this results in a good matching, it limits imaging to narrow-band applications, where only single nuclei based image can be created. In order to create an image based on other nuclei RF coils need to be replaced, which is not feasible in clinical applications. Magnetic field in current loop can be estimated in each direction using equations derived by Simpson et al. in *Simple Analytic Expressions for the Magnetic Field of a Circular Current Loop* [3]:

Magnetic field along the axis of a circular current loop:

$$B_z = \frac{\mu_0 I a^2}{2(a^2 + z^2)^{3/2}} \quad (1.3)$$

Magnetic field components near the axis ( $x, y \ll a$ ):

$$B_x = \frac{3a^2 \mu_0 I x z}{4(a^2 + z^2)^{5/2}} \quad (1.4)$$

$$B_y = \frac{3a^2\mu_0 Iyz}{4(a^2 + z^2)^{5/2}} \quad (1.5)$$

Magnetic field components far from the loop ( $r \gg a$ ):

$$B_r = \frac{\mu_0}{2\pi} \frac{(I\pi a^2) \cos \theta}{r^3} \quad (1.6)$$

$$B_\theta = \frac{\mu_0}{4\pi} \frac{(I\pi a^2) \sin \theta}{r^3} \quad (1.7)$$

where:

$B_{x,y,z}$  - Magnetic field along the axis n

$B_{r,\theta}$  - Radial and polar components of the magnetic field

$\mu_0$  - Permeability of free space

$I$  - Current in the loop

$a$  - Radius of the loop

$r$  - Distance from the center of the loop

$z$  - Distance along the axis from the center of the loop

$x, y$  - Small displacements from the axis

$\theta$  - Polar angle with respect to the axis of the loop

### Control system

Combines all necessary electronics and software to operate the MRI. This includes signal acquisition, RF amplifiers, gradient power supplies, frequency synthesizers, digital image processing system and user interface.

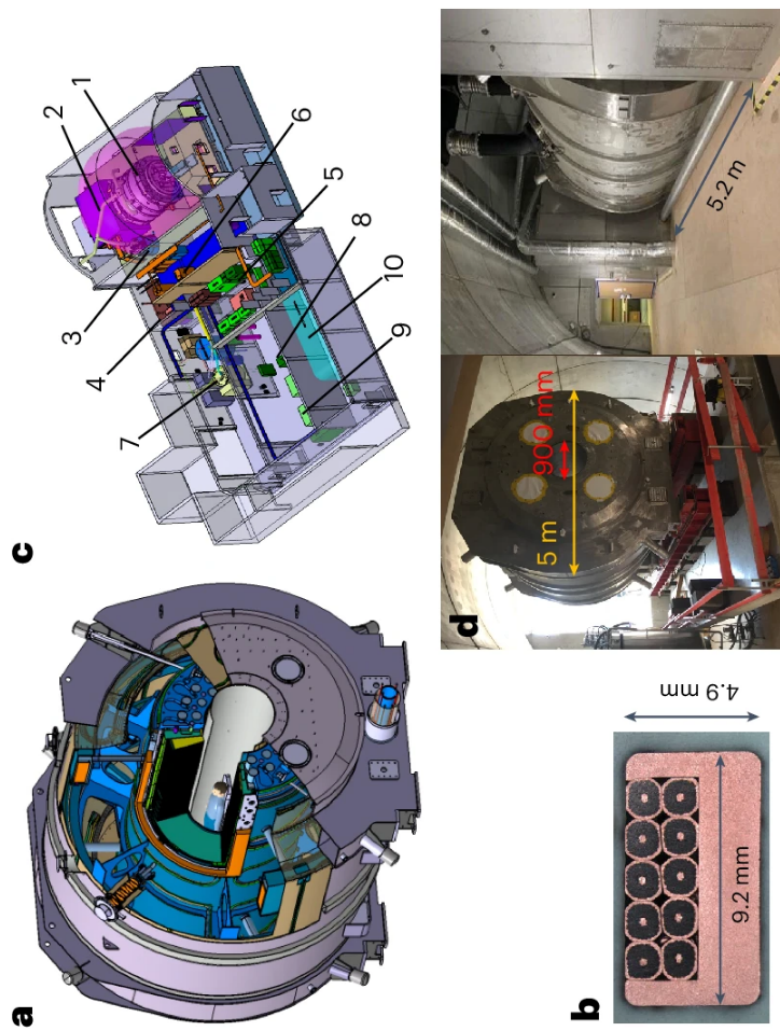


Figure 1.1: *Iseult* project. MRI with highest static magnetic field in use. Source: Figure 1 from Boulant, N., Mauconduit, F., Gras, V. et al. In vivo imaging of the human brain with the *Iseult* 11.7-T MRI scanner. Nat Methods 21, 2013–2016 (2024). <https://doi.org/10.1038/s41592-024-02472-7>

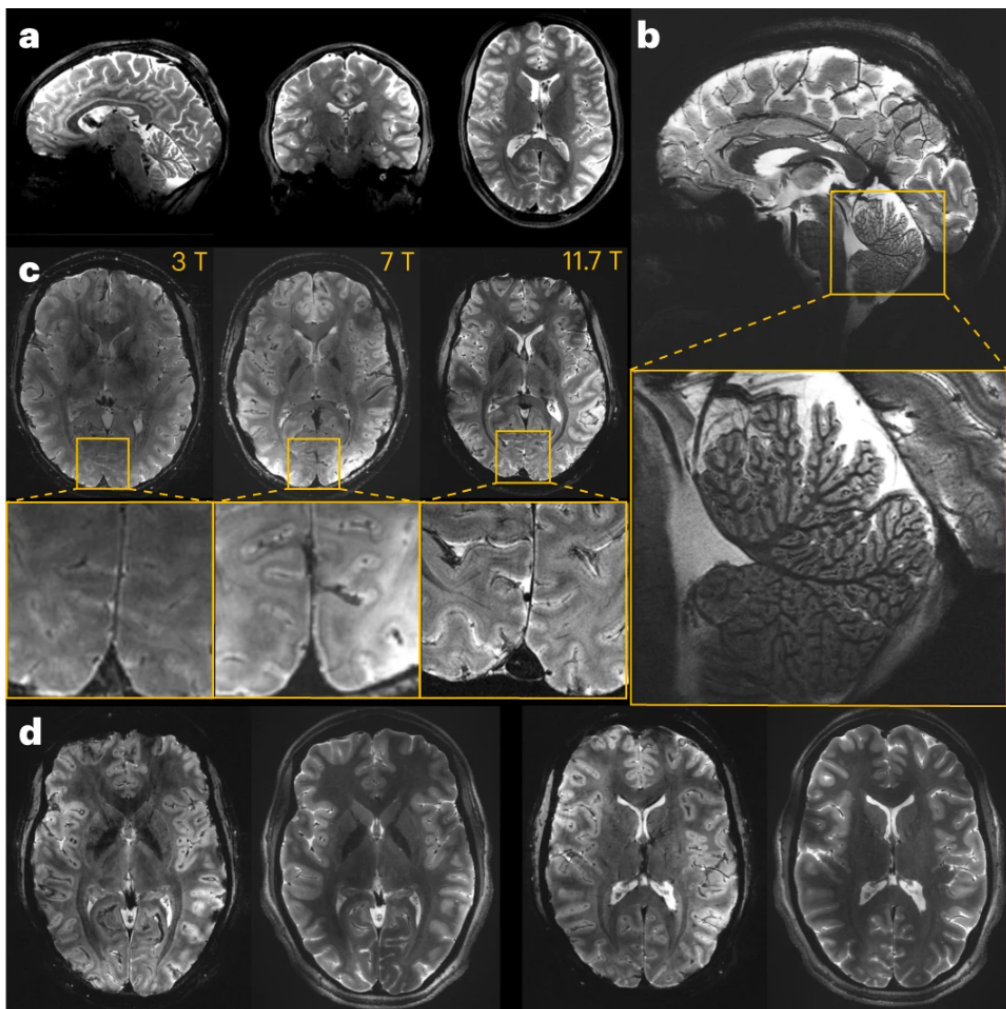


Figure 1.2: Differences in MRI  $^1H$  images based on the strength of a primary static magnetic field. Source: Figure 2 from Boulant, N., Mauconduit, F., Gras, V. et al. In vivo imaging of the human brain with the Iseult 11.7-T MRI scanner. Nat Methods 21, 2013–2016 (2024). <https://doi.org/10.1038/s41592-024-02472-7>

### 1.1.2 Principles of image generation

Image generation begins with placing a patient in the uniform magnetic field generated by the primary magnet. This results in magnetization of protons inside the tissues to align parallel to the magnetic field. The magnetization ( $M_0$ ) is proportional to the static field strength ( $B_0$ ):  $M_0 \propto B_0$  [2].

During image creation a RF pulse is emitted from the transmitter coil. This creates a phase coherence in proton spin rotation. This tips the longitudinal magnetization ( $M_z$ ) into xy-plane, creating phase coherence. Pulse duration and amplitude is set to achieve precise 90° rotation.

After excitation, the transverse magnetization ( $M_{xy}$ ) decays due to T2\* relaxation, while longitudinal magnetization ( $M_z$ ) recovers via T1 relaxation. Differences in T1 and T2 times between tissues results in image contrast. Additionally, gradient magnetic fields are generated in all directions (x,y,z) to spatially encode the signal. This allows to accurately localize the signal coming from the excited atoms.

### 1.1.3 Practical implications of using different nucleus in imaging

The key question answered by Hu et al. in “X-nuclei imaging: Current state, technical challenges, and future directions” [4] is the purpose of using different nucleus in MRI. As described, MRI images can provide different information about the body and disses, ex.

- $^{17}\text{O}$  - Oxygen might be a measure of physiological changes in the brain found in Alzheimer’s, Parkinson’s or Huntington’s disses.
- $^{19}\text{F}$  - Fluorine acts as a tracker for inflammation or drug delivery
- $^{23}\text{Na}$  - Sodium has been frequently applied to investigate diseases such as stroke, tumor or multiple sclerosis.

Each nuclei has it's own specific resonance frequency. MRI tuning defines the nuclei of interest in image creation as shown in 1.1.1. Tissues in human body primarily consists water and fat, making the hydrogen a most suitable nucleus for image generation in clinical applications. Few other nuclei such as  $^{13}\text{C}$ ,  $^{19}\text{F}$ ,  $^{23}\text{Na}$ , and  $^{31}\text{P}$  are used in drug delivery research, metabolic studies and other specialized applications. As described in Journal of Magnetic Resonance Imaging [4], due to physiology of a human and metabolic processes, there are other desired nuclei to be used in MRI which would give significant improvement in diagnosis, such as  $^{35}\text{Cl}$ ,  $^{39}\text{K}$ ,  $^{17}\text{O}$  or  $^{15}\text{N}$ .

Table 1.1 summarizes nuclei properties in terms of MRI characterization. Presented set of elements gives the frequency range for further consideration.

Table 1.1: Nuclear properties and Larmor frequencies at 3 T ordered by  $f_{larmor}$

Nucleus	$\gamma$ (MHz/T)	$f_{larmor}$ at 3 T (MHz)
$^1\text{H}$	42.58	127.7
$^{19}\text{F}$	40.08	120.2
$^{31}\text{P}$	17.24	51.7
$^{23}\text{Na}$	11.26	33.8
$^{17}\text{O}$	-5.77	17.3
$^{15}\text{N}$	-4.32	12.96
$^{35}\text{Cl}$	4.17	12.5

Negative value of gyromagnetic ratio for some of the nucleus is a result of anti-parallel orientation of it's magnetic momentum ( $\mu$ ) and intrinsic angle momentum ( $I$ ) as presented by M.Graves in the lecture "The Physics of MRI"<sup>5</sup>, with a relation between them being:

$$\gamma = \frac{\mu}{I} \quad (1.8)$$

These are only few of elements that can be used in MRI, yet it is clear that extending the device limitations makes it more versatile and potentially increases it's value in diagnostics. Figures 1.3 and 1.4 shows the differences between imaging with different nucleus.

## 1.2 Conventional MRI limitations

The main limitation of conventional MRI is in the narrow-band operation of RF coils. As described in 1.1.1, these coils are typically simple LC oscillator circuits with no practical method to tune them across a broad frequency range (e.g., 12 MHz to 128 MHz). When

<sup>5</sup>The Physics of MRI <https://www.bohndieklab.org/wp-content/uploads/2018/01/Lecture-3-5-MR-Physics-Handout.pdf>

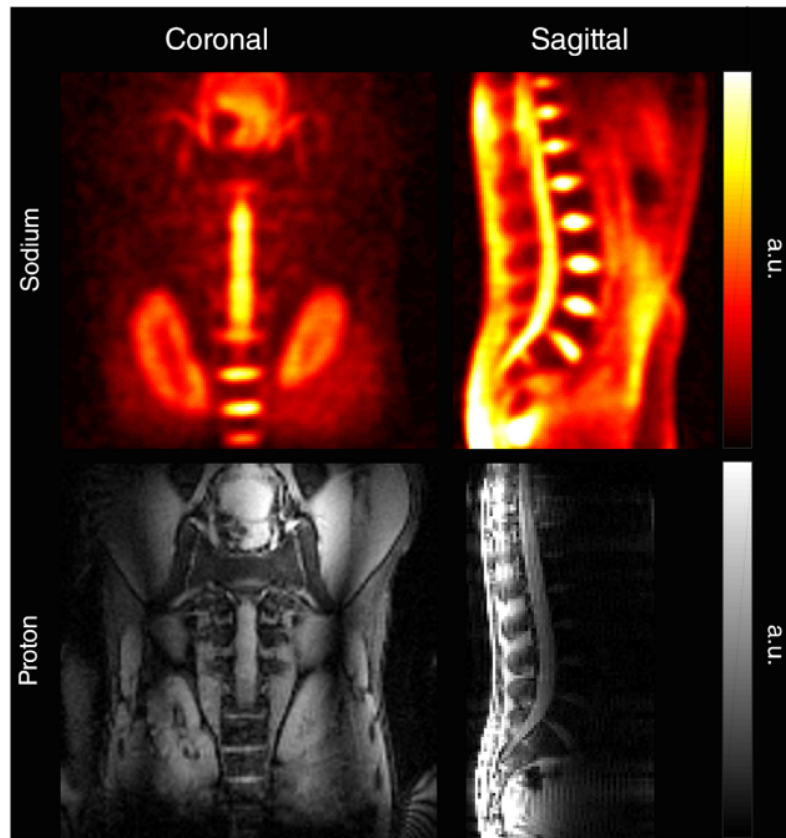


Figure 1.3: Spine MRI of a healthy volunteer. *"Both kidneys, inter vertebral discs, and the spine are clearly visible on  $^{23}\text{Na}$  image."* Source: Figure 1 from X-nuclei imaging: Current state, technical challenges, and future directions

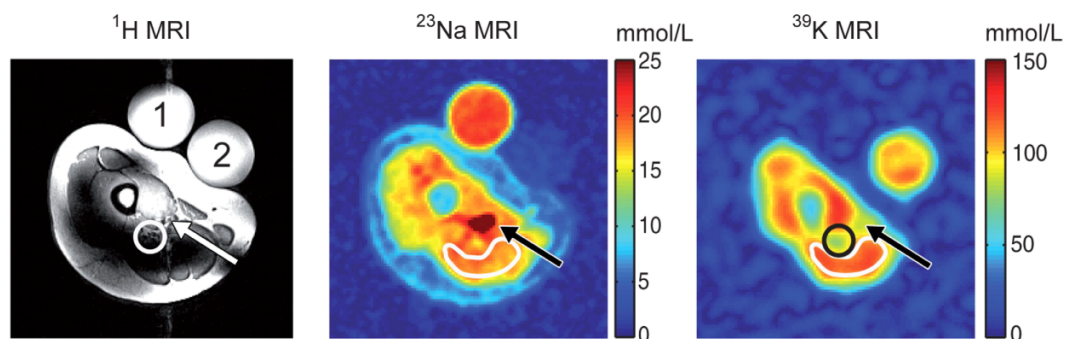


Figure 1.4: Thigh muscle MRI of a healthy volunteer. *"Regions of interest encircled in white show muscle tissue. The arrows indicate the position of the femoral artery and vein with high  $^{23}\text{Na}$  concentration. The black circles emphasize a low  $^{39}\text{K}$  concentration in the fatty tissue that surrounds the ischiadic nerve."* Source: Figure 11 from X-nuclei imaging: Current state, technical challenges, and future directions

an RF coil is tuned to a different frequency, to achieve the same  $B_1$  at lower frequencies, it is required to use amplification resonant circuit as shown by Han et al. [1]. This additional circuit is inherently limited in bandwidth by the Bode-Fano limit, to hundreds of kHz and covers the resonance of a single nucleus.

A solution to this challenge emerged with the advent of gallium nitride (GaN) semiconductors, which enable high-speed switching (exceeding 200 MHz) and high-current handling (over 20 A peak) in field-effect transistors (FETs) [5]. Victor Han, Miriam Hernández-Morales, and Chunlei Liu proposed a novel approach to overcome RF coil limitations through their development of the \*Any-nucleus distributed active programmable transmit coil\* (ADAPT coil) [1]. By replacing traditional tuning capacitors with GaN FET-based programmable switches, the ADAPT coil enables broadband operation without physical component adjustments. A detailed analysis of the ADAPT coil is provided in chapter 2.

## 2 ADAPT coil analysis

### 2.1 ADAPT overview

Han et al. in “Any-nucleus distributed active programmable transmit coil” [1] proposed the solution to create a broadband, programmable RF coil, that can operate at any relevant frequency. First, the tuning capacitor is replaced with H-bridge connecting the coil to the DC voltage source. Driving the coil alternatively by consecutive switches induces AC current thru the coil. Next, coil is divided into smaller segments, decreasing inductance per driven segment. Base configuration of ADAPT coil divides it in half, each half is driven by a separate switch in an alternating manner, with EPC21601 IC[6] acting as a switch. This results in AC current produced in the coil similarly to H-bridge configuration, however it advantages over H-bridge as it’s possible to continue scaling ADAPT coil by adding more switches and dividing coil into segments.

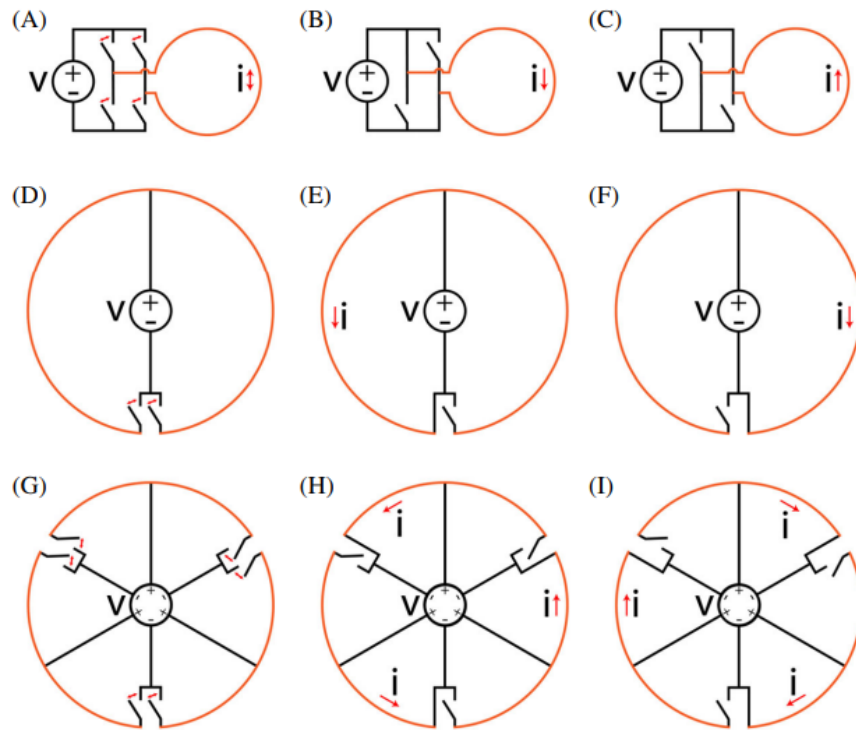


Figure 2.1: Schematic representation of ADAPT coil. Source: “Any-nucleus distributed active programmable transmit coil” | Figure 1G-I from [1]

This approach allows for current optimization by minimizing the segment inductance, and provides a feasible way of driving the coil at arbitrary X-nuclei frequency.

#### 2.1.1 EPC21601 in the ADAPT Coil

ADAPT coil proposed in [1] uses EPC 21601 IC with an integrated FET and a driver. This minimizes the design complexity of the circuit and has proven to give a satisfactory results in a fabricated ADAPT coil. Table 2.1 summarizes key ratings for the EPC21601 IC used in the ADAPT coil. For details, refer to the EPC21601 datasheet.

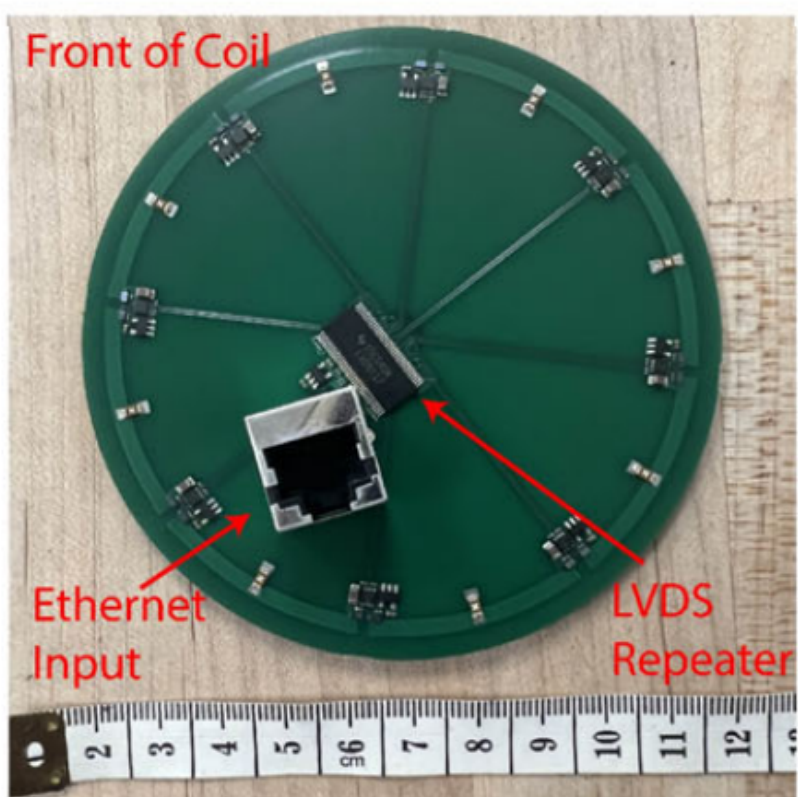


Figure 2.2: Fabricated ADAPT coil. Source: “Any-nucleus distributed active programmable transmit coil” | Figure 6 from [1]

Symbol	Definition	MIN	MAX	UNIT
$V_D$	Drain Voltage		40	V
$I_D$	Peak Drain Current		15	A
$t_{D(on)}$	Turn on delay time	3.5	6.75	ns
$t_F$	Drain fall time	0.75	1.5	ns
$t_{D(off)}$	Turn off delay time	3.2	5.5	ns
$t_R$	Drain rise time	0.32		ns
$t_{D(minon)}$	Minimum drain pulse width	1.5		ns

Table 2.1: Selected Absolute Maximum Ratings: EPC21601 IC used in ADAPT coil  
Source: EPC21601 datasheet

## 2.2 Advantages of ADAPT architecture

### Lowered segment inductance

By dividing a coil into smaller segments driven by single switch, the inductance is effectively lowered, which leads to the peak voltage being lowered proportionally. When voltage is lowered the segment can be driven at higher current, what brings the voltage peak to the same level, however increasing the current increases the magnetic field generated by the segment as presented in equations for coil magnetic fields in 1.1.1.

$$V = L \frac{di}{dt} \quad (2.1)$$

Lower  $L$  value allows for higher changes  $\frac{di}{dt}$  under a fixed voltage  $V$ , enabling higher peak currents, leading to higher magnetic field generated by the coil.

### Increased current

In adapt coil driving 10 nH segment can result in over 1.5 A current per segment, while driving 200 nH segment at the same frequency gives the current output of  $I < 150 \text{ mA}$ .

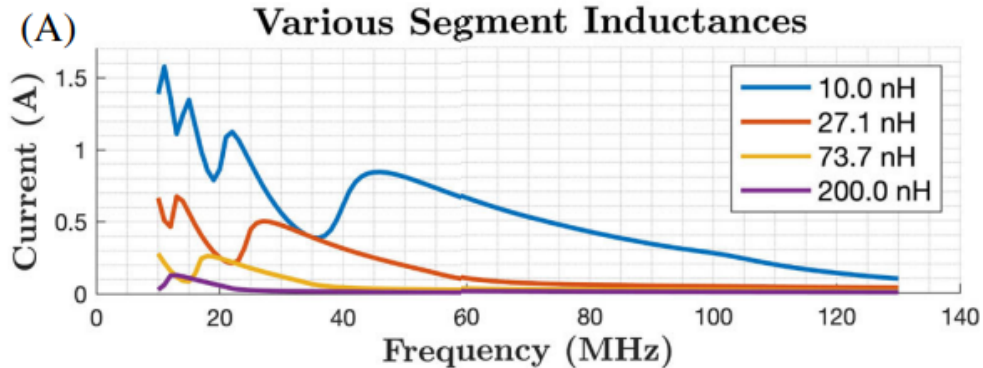


Figure 2.3: Current vs frequency, dependency on segment inductance in ADAPT coil.  
Source: "Any-nucleus distributed active programmable transmit coil" | Figure 4A from [1]

### Scalability

ADAPT design makes it easily scalable. This relates to lowering the segment inductance and its consequences. It is desired to drive low inductance, as shown on figure 2.3. To decrease the inductance in ADAPT coil segment it's as simple as dividing it into smaller segments that are being driven. However, scalability in ADAPT coil means that the coil can be made almost of any arbitrary total coil size without sacrificing the performance.

## 2.3 Limitations of ADAPT coil

### EPC 21601 maximum voltage

Han et al. estimates the peak voltage for the two border frequency elements,  $^1\text{H}$ : 127.7 MHz and  $^{15}\text{N}$ : 12.95 MHz. It is clear that with selected EPC 21601 IC the maximum voltage limit of 40 V (EPC 21601 selected parameters are presented in table 2.1), and resulting current limit, is quickly achieved. This limits the maximum magnetic field of ADAPT coil, resulting in low resolution imaging.

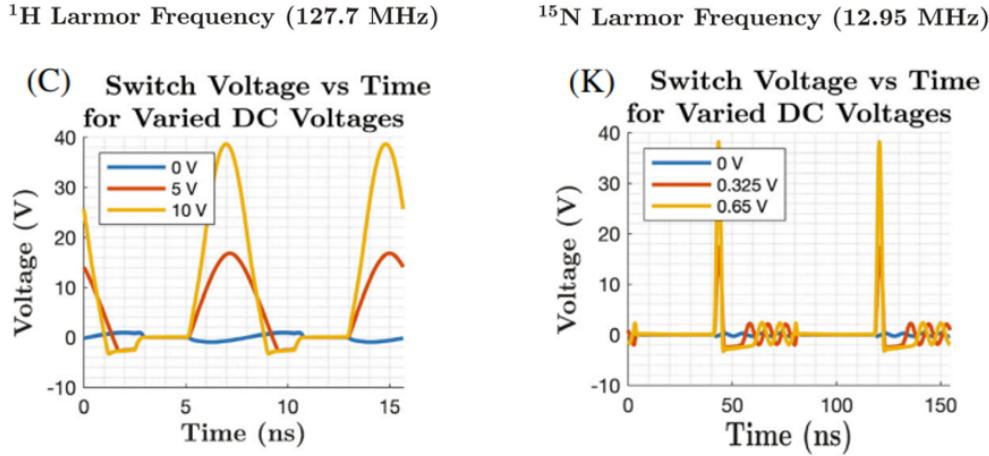


Figure 2.4: Peak voltage, dependency on supply voltage in ADAPT coil. Source: “Any-nucleus distributed active programmable transmit coil” | Figure 5C,K from [1]

The result of this voltage limit is the maximum theoretical magnetic field generated by the 9 cm ADAPT coil presented in [1] calculated using equation 1.3:

$$B_{z,max} @ 127.7 \text{ MHz} = \frac{\mu_0 I a^2}{2(a^2 + z^2)^{3/2}} = 21.52 \mu\text{T} \quad (2.2)$$

$$B_{z,max} @ 12.95 \text{ MHz} = \frac{\mu_0 I a^2}{2(a^2 + z^2)^{3/2}} = 43.04 \mu\text{T} \quad (2.3)$$

for:

- $\mu_0 = 4\pi \cdot 10^{-7} \frac{\text{N}}{\text{A}^2}$
- $I @ 127.7 \text{ MHz} \approx 2 \text{ A}$  - Simulated current output at  $^1\text{H}$  Larmor frequency (Figure 5A from [1])
- $I @ 12.95 \text{ MHz} \approx 4 \text{ A}$  - Simulated current output at  $^{15}\text{N}$  Larmor frequency (Figure 5I from [1])
- $a = 4.5 \cdot 10^{-2} \text{ m}$  - ADAPT coil radius
- $z = 19.6 \cdot 10^{-3} \text{ m}$  - Distance from the coil center at which actual measurement was performed in fabricated ADAPT coil

Values measured by Han et al. are within the calculated theoretical limits for both frequencies. However, the currents corresponding to measured magnetic fields are unclear. Presented values of supply voltage for the lower frequency bound would exceed the limits of the switches according to simulations for  $^{15}\text{N}$  and  $^{13}\text{C}$ . It is assumed that measured

values shown in ADAPT paper on the Figure 6[1] correspond to maximum supply voltage at given frequency.

### **Segments number**

In given shape, expanding of the coil is tied 8 segments per expansion. This is due to SN65LVDS117DGG LVDS repeater [7] used, which has 16 differential outputs (2x 8 off phase outputs for 8 segments), therefore to maximize the layout efficiency adding additional repeater requires adding 8 segments.

### **Connector current rating**

Presented ADAPT layout uses regular Ethernet socket SS-60000-008 with current rating of 1.5 A[8], but the total current for 8 segments, depending on the frequency, can sum up from 16 A to 32 A. Even if accounted for periodic operation of the coil (duty cycle < 100%), the current that the socket can handle. For 10% duty cycle (e.g. 10ms pulse every 100ms), pulsed current rating is:

$$I_{\text{pulsed}} \approx I_{\text{continuous}} \sqrt{\frac{100\%}{\text{DutyCycle}}} = 1.5 \text{ A} * \sqrt{\frac{100\%}{10\%}} = 4.74 \text{ A} \quad (2.4)$$

Driving higher current through the socket would lead to overheating, increased contact resistance, decreased performance and decreased lifetime.

## **2.4 Scope of ADAPT improvements - ADAPT module**

As described, ADAPT limitations are primarily a result of selected components for the coil fabrication. Hence, further considerations of extending ADAPT capabilities are focused on solving these physical limitations, selecting components that results in increased performance - higher current throughput, with stronger magnetic field as an outcome. Improved ADAPT coil is further referred to as ADAPT module.

### **2.4.1 Design requirements for improved ADAPT coil**

The goal of this work is to extend the power rating (with resulting magnetic field) of the ADAPT coil and redesign the coil for scalability up to full body coil. Parameters introduced in table 2.2 are considered a design point for ADAPT module, which should result in increased performance of the coil.

<b>Parameter</b>	<b>Symbol</b>	<b>Requirement</b>	<b>Notes</b>
Drain-Source Voltage	$V_{DS}$	$\geq 80 \text{ V}$	Minimum breakdown voltage
Drain Current	$I_D$	$\geq 2 \text{ A}$	Minimum current handling
Minimum Frequency	$f_{\min}$	10 MHz	Lower operational limit
Maximum Frequency	$f_{\max}$	130 MHz	Upper operational limit
Rise / Fall time	$t_r/t_f$	$\leq 1 \text{ ns}$	Maximum switching times

Table 2.2: Key design requirements for ADAPT coil module



# 3 FET technologies and drivers for high-power MRI systems

## 3.1 FET selection criteria

Key element of the ADAPT coil design is the Field Effect Transistor (FET) that acts as a switch. As discussed by Han et al. and in chapter 2 of this paper, for a FET to drive efficiently the coil there are few key characteristics that this device should have, namely:

- $f$  - switching speed frequency
- $I_D$  - drain maximum current
- $V_{DS}$  - maximum drain to source voltage
- $R_{DS,on}$  - channel resistance when FET is conducting

with drain voltage and frequency usually being used to compare different devices. Depending on the material and the topology of a FET these will differ significantly. These are also the parameters that directly defines the performance of a ADAPT coil. In this chapter, different FET technologies are compared to review common and available materials along with emerging technologies that potentially might give a significant breakthrough in the overcoming of limitations in ADAPT coil design and as a result - limitations of MRI.

## 3.2 FET critical characteristics

### Voltage rating

Switching inductive loads (e.g., MRI coils) induces voltage spikes due to  $V_L = L \frac{di}{dt}$ . To protect the FET's drain terminal (when driving the low side), ensure:

- The peak voltage remains below the FET's absolute maximum rating

or

- Use a pin diode to clamp transient voltages, as implemented in the ADAPT coil.

### Current rating

The magnetic field strength ( $B$ ) is proportional to coil current ( $I$ ) as shown in 1.1.1 ( $B \propto I$ ). Therefore, it is necessary to select FETs with sufficient pulsed current rating, as MRI is driven at high frequency.

### Gate charge

FET transistor gate requires non zero charge  $Q_G$  to control the transistor. The driver's current rating depends on this value, as:

$$I = \frac{Q_G}{t} \quad (3.1)$$

## 3.3 FET for MRI power electronics

Two main general categories of field effect transistors are[9]:

1. JFET - Junction Field Effect Transistor
2. MOSFET - Metal Oxide Semiconductor FET

Additionally, more advanced types of transistor extends the design to achieve higher operation parameters, like High Electron Mobility Transistor (HEMT). HEMT extends the layout of channel, adding additional barrier and space layers (figure 3.1 below), formed with wider band gap material than channel layer [10] which directly translates to increased performance. Commonly used in HEMT are Gallium (Ga) based materials: e.g. Gallium Nitride (GaN) or Aluminium Gallium Arsenide.

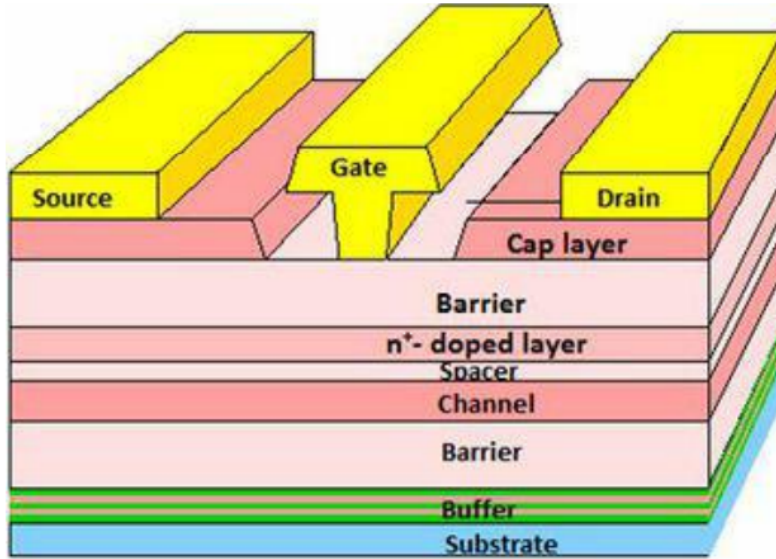


Figure 3.1: General structure of HEMT device. Source: *A Review Study on Fundamentals of HEMT Device and Technology* | Figure 1 from [10]

### 3.3.1 Diamond interfaced TMO

There are emerging types like transition-metal oxide transistors interfaced with diamonds (TMOD) discussed by Yin et al. in “Enhanced transport in transistor by tuning transition-metal oxide electronic states interfaced with diamond”. In the fabricated TMOD FET hole mobility achieved was  $\mu_p = 20.2 \frac{cm^2}{Vs}$ . This translates to maximum frequency, estimated with equation derived in “Limitations of the intrinsic cut-off frequency to correctly quantify the speed of nanoscale transistors” [12]:

$$f_T \approx \frac{\mu_p \cdot V_{DS}}{2\pi L^2} \quad (3.2)$$

where:

$\mu_p$  - Hole mobility  $\frac{cm^2}{Vs}$

$V_{DS}$  - Drain-source voltage V

$L$  - Channel length m

#### Frequency range

For discussed fabricated TMOD with:

- $\mu_p = 20.2 \frac{cm^2}{Vs}$
- $V_{DS} = 20 V$  - assumed value for drain-source voltage
- $L = 10 \mu m$  - minimum channel length presented in [11]

the cut-off frequency is estimated to be:

$$f_T = \frac{20.2 \frac{\text{cm}^2}{\text{Vs}} \cdot 20 \text{V}}{2\pi(10\mu\text{m})^2} = 64.3 \text{ MHz}$$

The  $V_{DS}$  value is not explicitly stated in the [11], therefore approximated value is used based on the assumption that this type of the FET should operate within the limits of other TMO devices and other types of FET. Additionally, value of  $V_{DS} = 20 \text{ V}$  is chosen to be relatively low to ensure conservative operation, however it is advised to treat this value only as an example as it will most likely differ in fabricated device, depending on a final design of a FET.

### Thermal performance

Moreover, diamond interface in TMO ensures exceptional heat dissipation in high-power application with its extreme thermal conductivity  $1800 \frac{\text{W}}{\text{mK}} \leq K_{diamond}$  [13] compared to GaN's up to  $\approx 250 \frac{\text{W}}{\text{mK}}$  [14] at 300 K.

### Breakdown voltage

Diamond has exceptional breakdown voltage of  $V > 10 \text{ MV}$ , well exceeding GaN at around 3 MV. This high value is due to diamond's ultra-wide bandgap of 5.5 eV[15].

Properties of materials was done by Zhao et al. in [15], highlighting the key differences.

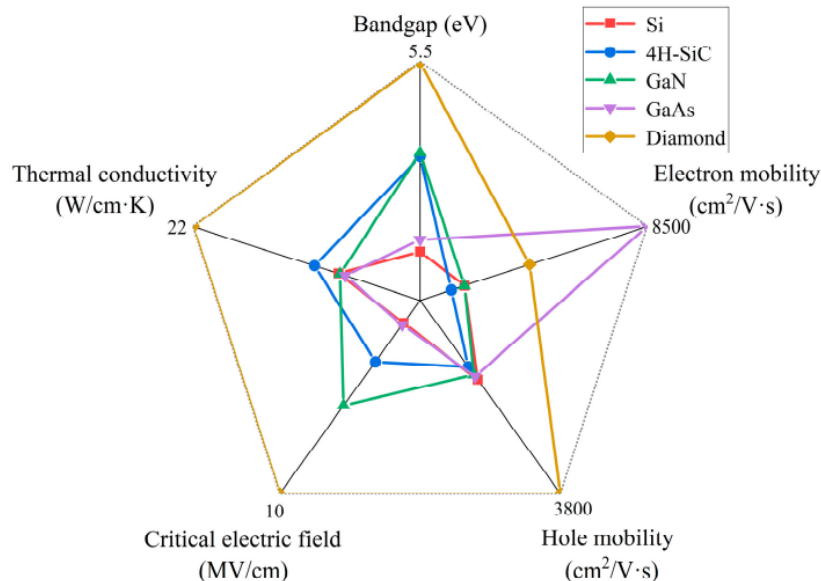


Figure 3.2: Comparison of diamond properties with other materials. Source: [15] | Figure 1 from [15]

All these properties suggest that diamond interfaced TMO FET should outperform GaN FET in high-power applications. When the technology becomes more mature and the manufacturing process will allow to produce sub-micrometer channel TMOD FET the frequency will increase drastically. This could result in a new branch of high-power RF electronics. Unfortunately this technology is still in early stage and is not available in widely available packages.

### 3.3.2 Market available FET types

Considering mature (market available) technologies only Beheshti compares available devices by power rating and frequency of operation.

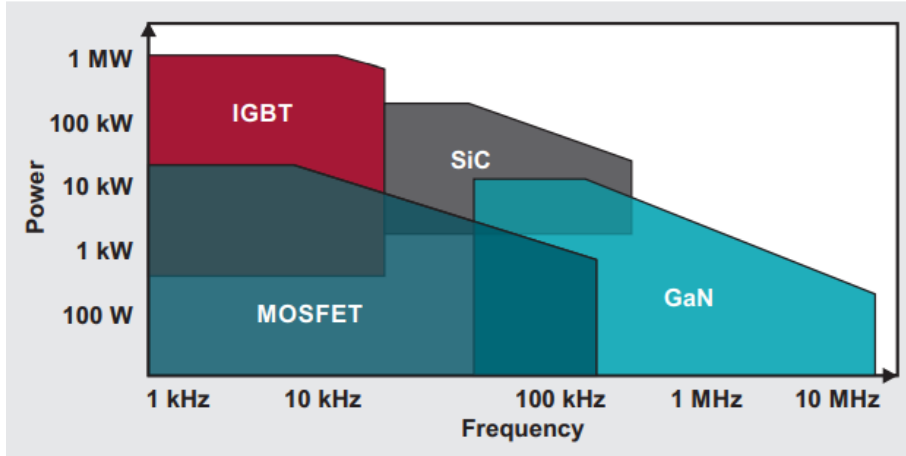


Figure 3.3: Comparison of high power FET types. Source: *Wide-bandgap semiconductors: Performance and benefits of GaN versus SiC* | Figure 1 from [16]

In table 3.1 parameters of FET types were compared.

Feature	IGBT	MOSFET	SiC	GaN	Diamond TMO Estimation
Operation frequency	> 10 kHz	> 100 kHz	> 100 kHz	> 100 MHz	> 1 GHz
Voltage Range [V]	1200	1200	1200	600	> 1000
Efficiency [%]	97.0	97.7	98.9	99.2	> 99
Power capability [kW]	> 1000	> 10	> 10	> 10	> 100
Power density [W/mm <sup>2</sup> ]	0.11	0.13	0.26	0.33	< 3.8
Switching Losses [W] @ 1kW load	9	9	7	4	< 1
Cost (Normalized to MOSFET)	0.4	1	2.4	1.3	N/A

Table 3.1: Comparison of Power Semiconductor Devices. Table based on [6, 9, 11, 13, 14, 15, 16, 17, 18, 19, 20, 21]

TMOD values are estimated or used are best reported values for early-stage research, added to highlight the potential of the technology, not used in further considerations.

All the FET types fulfills most of the requirements described in the table 2.2, however only GaN and TMOD can operate within high frequency range of wide-band MRI.

### 3.4 High performance driver devices

Switching a FET at high speed requires precise control signal. Primary concerns is the peak gate drive current defined as the change of the gate charge over time [22].

$$I_{drive} = \frac{dQ}{dt} \quad (3.3)$$

Value of the maximum current supported by the driver to source or sink directly defines how fast the FET can switch the load. If the switching is done in a continuous way, an

additional average gate drive current is defined as the gate charge in time expressed with switching frequency [22]:

$$I_{avg} = Q_G \cdot f \quad (3.4)$$

This value together with the voltage applied when driving the FET determines the power dissipation in the gate driver.

In the ADAPT coil the biggest challenge for designing the driving circuit is the inductive load (the coil) being switched. Reactance of a coil causes high inrush currents before the core magnetizes, governed by Faraday's law of induction, well described by Zawilak and Gwoźdiewicz in "Start-up of large power electric motors with high load torque". This phenomena is especially important in high-power applications where the high current change causes voltage peaks according to equation 2.1.

### 3.4.1 FET driver current requirements

When driving an FET at high speeds, several key parameters must be considered. At the Larmor frequency of  ${}^1H$  (127.7 MHz), the switching period is:

$$T = \frac{1}{f} = \frac{1}{127.7 \times 10^6 \text{ Hz}} = 7.8 \text{ ns.}$$

#### Rise/fall times

The rise and fall times ( $t_r, t_f$ ) of the transistor must satisfy:

$$t_r, t_f \leq \frac{1}{2}T = 3.9 \text{ ns.}$$

#### Gate drive current rating

Current rating required for a gate driver can be found using equation 3.5

$$I = \frac{Q}{t} \quad (3.5)$$

where:

- Q - total gate charge
- t - Rise/fall time

In integrated circuit like *EPC21601* where the driver is integrated with a transistor, proper current rating is done by the manufacturer. This parameter is important to take into the consideration when designing the circuit with discrete elements.

Example calculation is done for *EPC2221 GaN FET* driven with *TPM2025 gate driver*. From the datasheet we get:

- $Q_G = 0.85 \text{ nC}$
- $t_r = 0.45 \text{ ns}$
- $t_f = 0.45 \text{ ns}$
- $I_{sink,max} = 7 \text{ A}$
- $I_{source,max} = 5 \text{ A}$

then:

$$I_{source} = \frac{0.85 \text{ nC}}{0.45 \text{ ns}} = 1.89 \text{ A} < I_{source,max}$$

$$I_{sink} = \frac{0.85nC}{0.45ns} = 1.89A < I_{sink,max}$$

This confirms the driver is suitable for a selected FET. Exceeding these limits risks waveform distortion and reduced efficiency.

Advanced driver design strategies are described in the Smart Gate Driver paper [22] by Oborny and Ojha.

### 3.5 Integrated and discrete drivers

The driver of a FET can be supplied with together with the transistor in one package, like the EPC21601 IC, or it can be a discrete module, designed and fabricated in a separate package. The two approaches differs in implementation, each having advantages and disadvantages, ex. integrated driver has better performance due to minimized parasitic characteristics, but discrete driver usually can drive higher gate charges, so the switched voltage  $V_{DS}$  can be higher at the same frequency. When using discrete driver one should carefully consider the PCB layout of a switch. Xie and Brohlin provides the detailed analysis of the differences in the layouts in *Optimizing GaN performance with an integrated driver* [24] and describes the key parameters like gate-loop inductance or FET protection circuits.

EPC 21601 used in ADAPT coil is an integrated circuit of the FET and the driver. In chapter 2 the key limitations of this device were described. A few alternative IC like EPC 21603 or EPC 21701 were evaluated in terms of increasing the power output of a coil, yet having nearly the same footprint as EPC 21601, but neither has characteristics that could fulfill the requirements. Therefore a discrete driver approach was considered.

#### **EPC 21701**

EPC 21701 would solve the key limitation of EPC 21601 with it's drain voltage rating up to 80 V. However, stated nominal frequency of 50 MHz is well below the design point 2.2. It is unclear what's the actual frequency limit for this IC as provided value is guaranteed by design, but not tested, what is a main reason to disregard this IC in further considerations.

## 3.6 Device selection and validation

### 3.6.1 FET selection

The review was done on market available FET devices. There are few outstanding manufacturers like Efficient Power Conversion Corporation and Infineon Technologies Company that provides variety of FETs with high performance. All FETs are compared for drain voltages, current rating and gate charge. Calculated is gate drive current requirement based on equation 3.3 with assumption of rise / fall time  $t_r/t_f = 0.5\text{ ns}$ .

#### **EPC 2012C**

EPC 2012C is an enhanced-GaN single FET in a 1.7mm x 0.9mm package. It has exceptional maximum ratings of drain voltage  $V_{DS} = 200\text{ V}$  and pulsed drain current  $I_D = 22\text{ A}$ .

$$I_{drive} = \frac{1\text{ nC}}{0.5\text{ ns}} = 2\text{ A} \quad (3.6)$$

and average currents at boundary frequencies of:

$$I_{avg@127.7MHz} = 1\text{ nC} \cdot 127.7\text{ MHz} = 127.7\text{ mA} \quad (3.7)$$

$$I_{avg@12.95MHz} = 1\text{ nC} \cdot 12.95\text{ MHz} = 12.95\text{ mA} \quad (3.8)$$

Parameter	Symbol	Value
Drain-Source Voltage	$V_{DS}$	200 V
Pulsed Drain Current	$I_{D(pulsed)}$	22 A
Total Gate Charge	$Q_G$	1 nC
On-Resistance	$R_{DS(on)}$	70 mΩ
Input Capacitance	$C_{ISS}$	100 pF
Gate Voltage	$V_G$	6 V
Price per unit (Digi-Key, 2025)	–	3.71 \$

Table 3.2: Key parameters of EPC2012C GaN FET

### EPC 2221

EPC 2221 is a double FET configuration. This gives a big advantage of using single package to drive 2 consecutive segments, reducing the complexity of the circuit and the total cost.

Parameter	Symbol	Value
Drain-Source Voltage	$V_{DS}$	100 V
Pulsed Drain Current	$I_{D,pulsed}$	20 A
Total Gate Charge	$Q_G$	0.85 nC
On-Resistance	$R_{DS(on)}$	40 mΩ
Input Capacitance	$C_{ISS}$	94 pF
Gate Voltage	$V_G$	6 V
Price per unit (Digi-Key, 2025)	–	3.55 \$

Table 3.3: Key parameters of EPC2221 GaN FET

$$I_{drive} = \frac{0.85 \text{ nC}}{0.5 \text{ ns}} = 1.7 \text{ A} \quad (3.9)$$

and average currents at boundary frequencies of:

$$I_{avg@127.7MHz} = 0.85 \text{ nC} \cdot 127.7 \text{ MHz} = 108.6 \text{ mA} \quad (3.10)$$

$$I_{avg@12.95MHz} = 0.85 \text{ nC} \cdot 12.95 \text{ MHz} = 11 \text{ mA} \quad (3.11)$$

EPC2221 IC is selected to proceed with ADAPT module.

### GS66516B

Infineon GS66516B is the highest rated FET in the comparison taken into account. It can handle extreme voltage and current compared to the other available FETs. The downside is its gate charge and the resulting drive current, which also greatly exceeds other devices. As described in following subsection 3.6.2, there are no available gate drivers that can handle the drive current. Especially the average current at high frequencies would most likely add a necessity of driver cooling, which would greatly increase the complexity of a design.

However, this FET is still considered, as if there emerge a gate driver IC, it can be easily switched to achieve very high magnetic fields with ADAPT coil, potentially moving to  $mT$  range from current  $\mu T$  range. This would increase greatly the resolution of MRI imaging with ADAPT coil.

Parameter	Symbol	Typical Value
Drain-Source Voltage	$V_{DS}$	650 V
Continuous Drain Current (25°C)	$I_D$	60 A
Pulsed Drain Current	$I_{D,\text{pulsed}}$	120 A
Total Gate Charge	$Q_G$	14.2 nC
On-Resistance	$R_{DS(on)}$	25 mΩ
Input Capacitance	$C_{ISS}$	518 pF
Gate Voltage	$V_G$	7 V
Price per unit (Mouser Electronics, 2025)	–	40.93 \$

Table 3.4: Key typical parameters of GS66516B GaN FET

$$I_{drive} = \frac{14.2 \text{ nC}}{0.5 \text{ ns}} = 28.4 \text{ A} \quad (3.12)$$

and average currents at boundary frequencies of:

$$I_{avg@127.7MHz} = 14.2 \text{ nC} \cdot 127.7 \text{ MHz} = 1.81 \text{ A} \quad (3.13)$$

$$I_{avg@12.95MHz} = 14.2 \text{ nC} \cdot 12.95 \text{ MHz} = 183.9 \text{ mA} \quad (3.14)$$

### 3.6.2 Driver selection

Market review showed a lack of FET drivers that can switch FETs with short rise and fall times. Usually, the driver would fulfill the switching speed criteria, but cannot withstand the drive current.

#### TPM2025/TPM2025Q

TPM2025 IC from 3peak Incorporated can operate with pulsed gate currents up to 5 A sink and 7 A source. Its rise / fall times are also within the design limits at 450 ps.

Parameter	Symbol	Typical Value
Supply Voltage	$V_{CC}$	5 V
Input Voltage Range	$V_{IN}$	0 V to 5 V
Output Source Current	$I_{\text{output, source}}$	5 A
Output Sink Current	$I_{\text{output, sink}}$	7 A
Rise Time	$t_{rise}$	0.45 ns
Fall Time	$t_{fall}$	0.45 ns
Minimum Pulse Width	$t_{PW, \text{min}}$	0.69 ns

Table 3.5: Typical parameters of TPM2025/TPM2025Q GaN Driver

TPM2025 can operate in alternative parallel source mode, where the source capability can be increased. Then, the limit of gate drive current will depend on the maximum sink current of 7 A.

TPM2025 is used in further design steps.

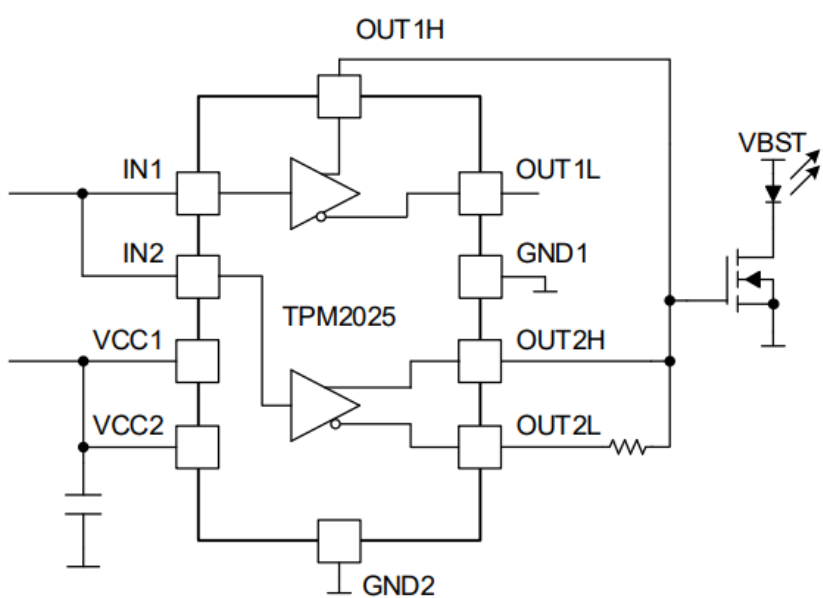


Figure 3.4: TPM2025 parallel driving mode. Source: [25] | Figure 14 from [25]



## 4 ADAPT Simulations

To compare the expected (simulated) performance of a ADAPT module, the simulations are setup in a same manner as was done in [1]. The investigation is done towards obtaining the functions in time of a current, voltage and a functions of supply voltage of current harmonics and current efficiency similarly to figure 5 in [1]. Current efficiency is defined by Han et al. as the ration of current in single segment to square root of total power delivered to the system:

$$\eta_{current} = \frac{I_{seg}}{\sqrt{P_{tot}}} \quad (4.1)$$

where:

$I_{seg}$  - current flowing in one coil segment

$P_{tot}$  - total power delivered to the coil

The impact of reducing the parasitic characteristics as well as segment inductance and resistance are shown in figure 4 from [1], therefore, these simulations were confirmed to be valid, but not developed further.

### 4.1 ADAPT coil baseline circuit simulations

First, the simulations for  $^1H$ ,  $^{13}C$ ,  $^{15}N$  from “Any-nucleus distributed active programmable transmit coil” were recreated to obtain the baseline values for a comparison. These simulations are performed for single segment (2 switches). EPC provides the SPICE model for the EPC 21601 IC together with the datasheet available at the product description page [26], containing the models for both FET and the driver of EPC 21601. Compared to the circuit in figure 2 from [1] there was major change of diode model, capacitor in series with resistor was replaced with a pin diode model available in Keysight ADS simulation software.

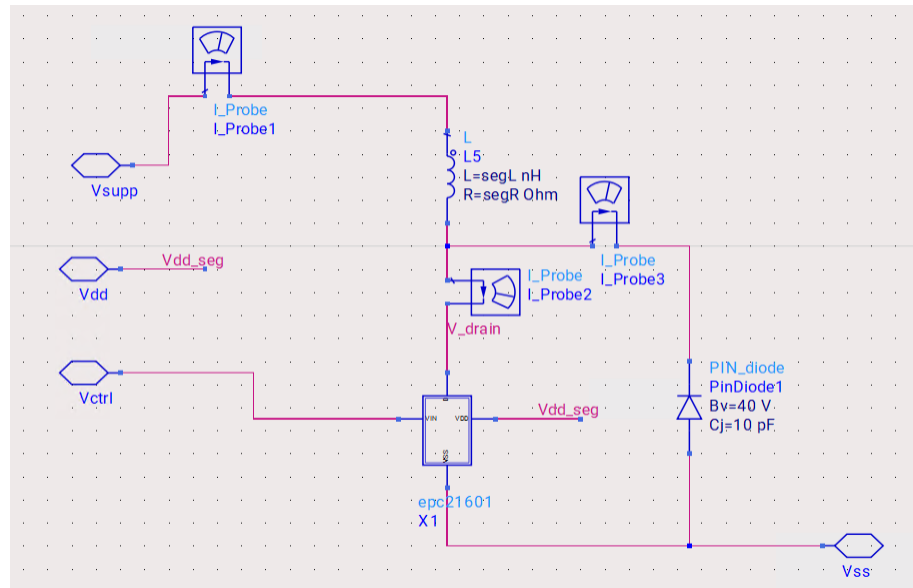


Figure 4.1: Segment arm model used in simulations.

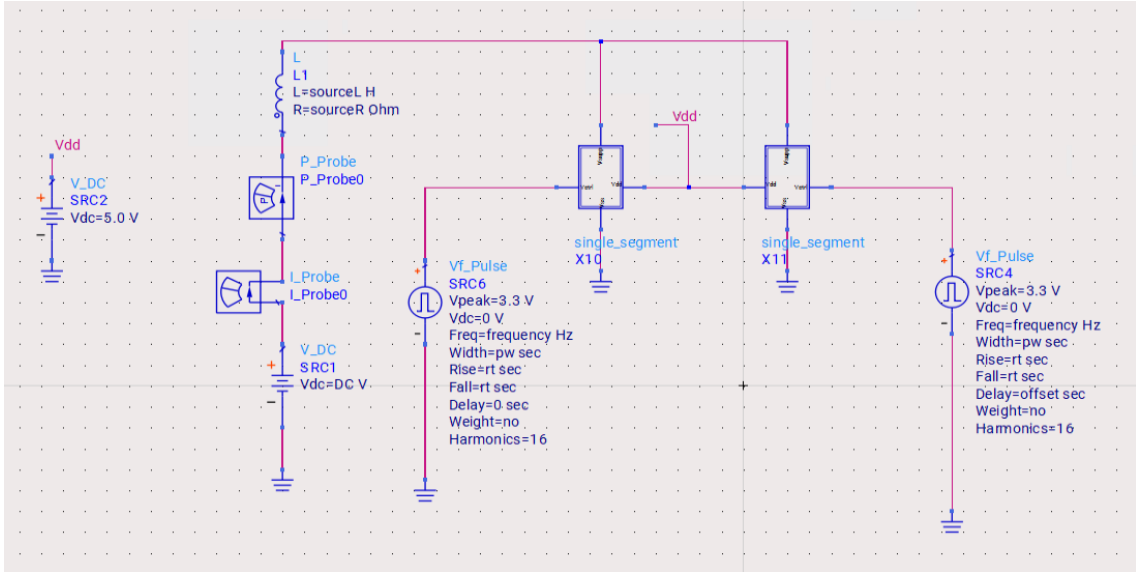


Figure 4.2: Simplified ADAPT segment used to recreate the baseline simulations results.

In the table 4.1 below are listed values for variables used across simulations for different nucleus. Maximum supply voltages were decreased below [1] levels, as introduction of pin diode in the circuit ADS model resulted in increased peak drain voltages, exceeding the EPC 21601 IC rating. Values to which the supply voltages were decreased were found experimentally.

Parameter	Unit	$^1H$	$^{13}C$	$^{15}N$
$L_{seg}$	nH	10	10	10
$R_{seg}$	$\Omega$	0	0	0
$L_{source}$	nH	100	100	100
$R_{source}$	$\Omega$	0	0	0
$f$	MHz	127.7	32.1	12.95
$t_r$	ns	1	1	1
$t_f$	ns	1	1	1
$skew$	ns	0	0	0
$V_{DC,max}$	V	8	1.2	0.65

Table 4.1: Comparison of  $^1H$ ,  $^{13}C$ , and  $^{15}N$  configurations

For all configurations the offset and pulse width were set to value in relation to frequency  $f$ , skew and rise/fall times  $t_r/t_f$ , calculated using following equations 4.2 and 4.3:

$$\text{offset} = \frac{1}{\frac{f}{2}} + \text{skew} \quad (4.2)$$

$$pw = \frac{1}{\frac{f}{2}} - t_r - t_f \quad (4.3)$$

Current and voltage plots were made for maximum supply voltage at each frequency. The theoretical magnetic field at each frequency was calculated using equation 1.3 for:

- $\mu_0 = 4\pi \cdot 10^{-7} \frac{N}{A^2}$

- $a = 4.5 \cdot 10^{-2} m$  - ADAPT coil radius
- $z = 19.6 \cdot 10^{-3} m$  - Distance from the coil center at which actual measurement was performed in fabricated ADAPT coil

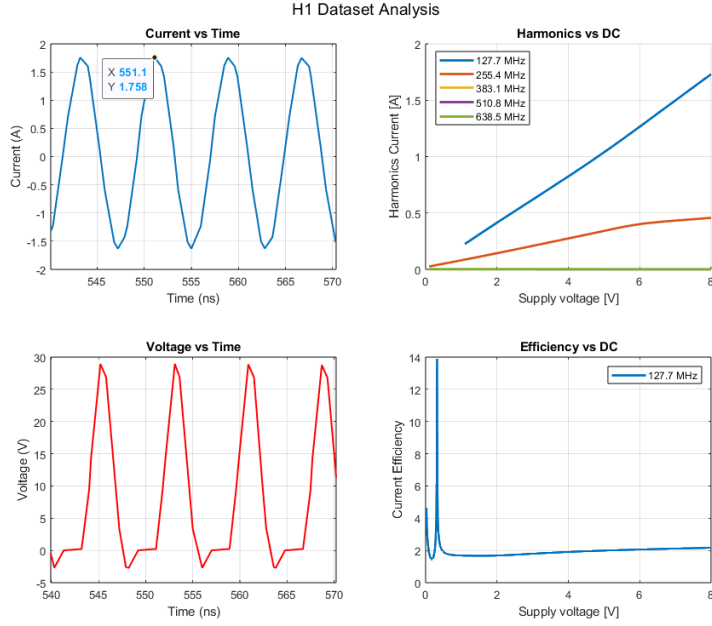


Figure 4.3:  $^1H$  simulation results. Compared to results presented in [1] there is visible difference in current efficiency value, due to introduction of more advanced diode model. At around  $V_{DC} \approx 0.4V$  the efficiency peaks at value  $14 \frac{A}{\sqrt{W}}$ . Peak voltage and current reduced due to lower supply voltage.

$$B_z = \frac{\mu_0 I a^2}{2(a^2 + z^2)^{3/2}} = 18.83 \mu T \quad (4.4)$$

for:

- $I \approx 1.75 A$

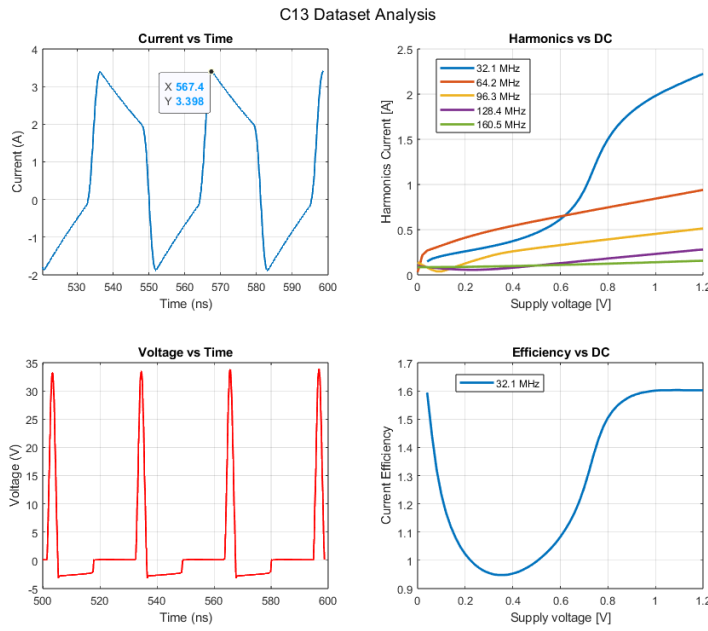


Figure 4.4:  $^{13}C$  simulation results.

$$B_z = \frac{\mu_0 I a^2}{2(a^2 + z^2)^{3/2}} = 36.6 \mu\text{T} \quad (4.5)$$

for:

- $I \approx 3.4 A$

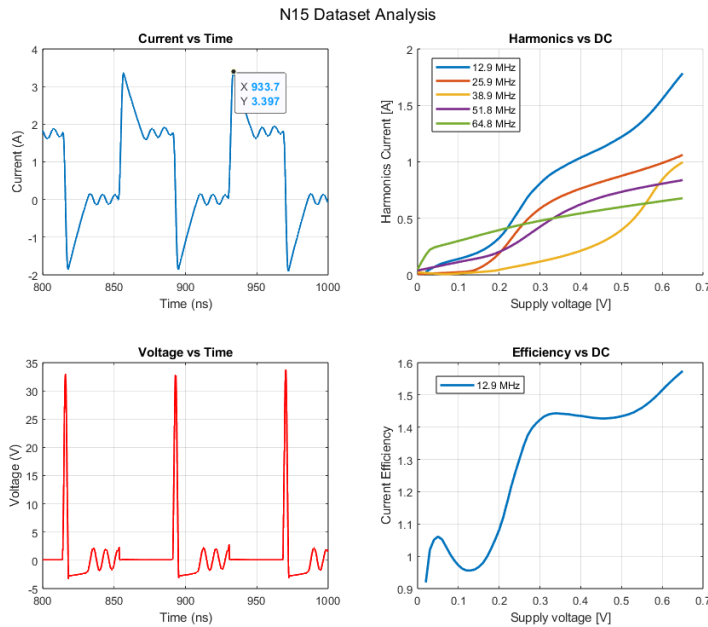


Figure 4.5:  $^{15}N$  simulation results. Peak voltage and current reduced due to lower supply voltage.

$$B_z = \frac{\mu_0 I a^2}{2(a^2 + z^2)^{3/2}} = 36.6 \mu\text{T} \quad (4.6)$$

for:

- $I \approx 3.4 A$

## 4.2 Magneto-static simulations

Following where the magneto static simulations of a ADAPT coil model using CST suite. There was no 3d model provided with [1], hence an approximated arbitrary model was created using Autodesk Inventor, further used in CST simulations. A S-Parameters model was obtained from the magneto-static simulations, to be further used in electro-magnetic co-simulations in Keysight ADS.

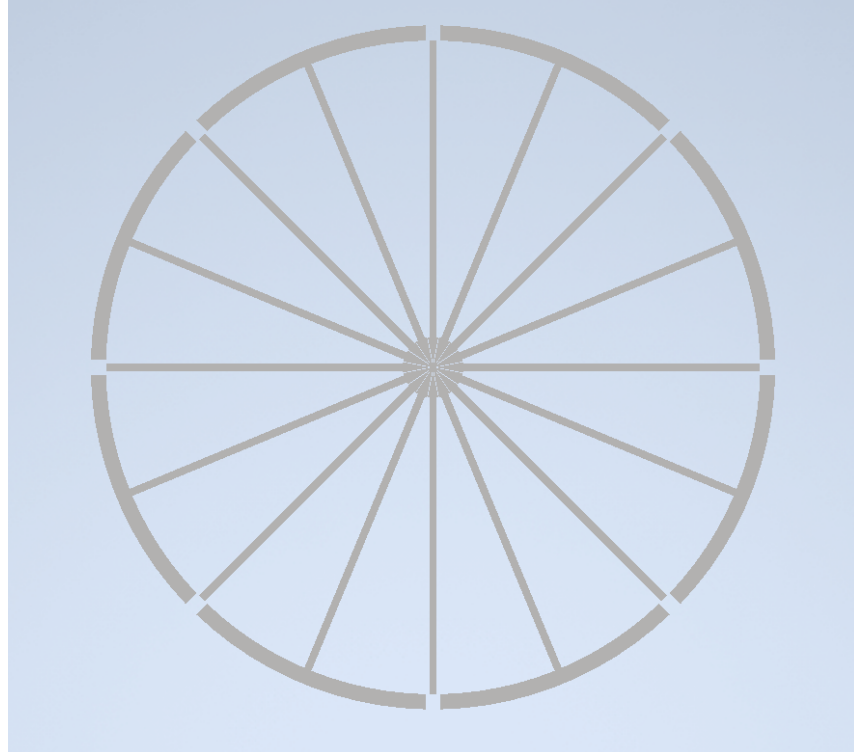


Figure 4.6: ADAPT 3D model front view, prepared for magneto-static simulations. Each part of the coil has  $0.5 \text{ mm}$  thickness. Gaps between consecutive segments are  $2 \text{ mm}$  wide. The  $9 \text{ cm}$  diameter is measured from the coil center to the outer side of a segment. Two supply planes are separated in the middle by a small gap.

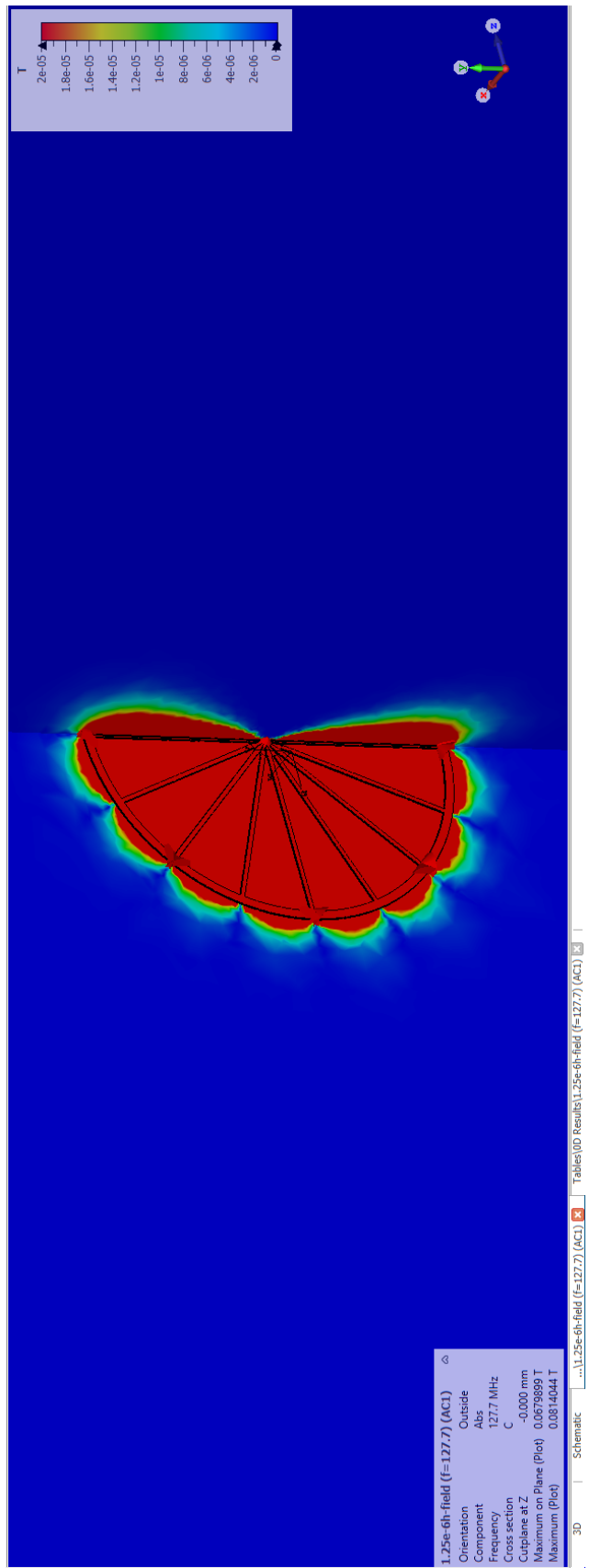


Figure 4.7: Result magnetic field of magneto-static simulation for ADAPT coil.

### 4.3 ADAPT coil module circuit simulations

ADAPT module is assumed to drive segments of the same inductance  $L_{seg} = 10 \text{ nH}$ . As described in subsection 3.6.1, the switch driving the segment is replaced with the EPC 2221 dual FET IC and the TPM2025 driver. According to TPM2025 characteristics rise and fall times will drop to  $t_r/t_f = 0.45 \text{ ns}$ . Major change in ADAPT module is removal of protection diode. This is done to remove diode capacitance, preventing unwanted resonance with a coil. To protect switch from excessive voltage spikes, supply voltage is adjusted to allow voltage peaks below safety threshold.

Additionally the control signal voltage is increased to  $5 \text{ V}$ . ADAPT module changes the supply path for the coil segments, each module has only one segment supplied, thus the minimum required module count is 2 (modules are interconnected). Additionally, modules are placed on a separate PCBs, hence from practical point of view the minimum number of modules is 4, further described in chapter 5.

#### 4.3.1 Simulation setup

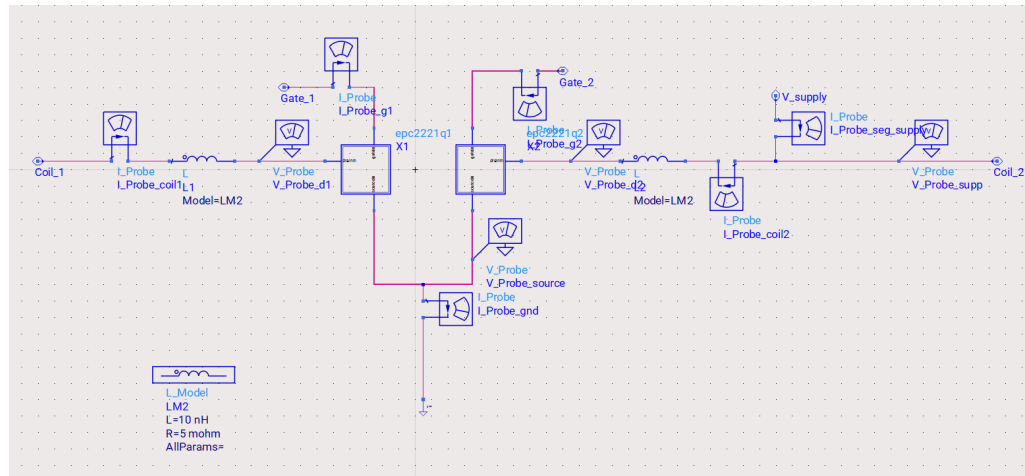


Figure 4.8: ADAPT module arm model used in simulations.

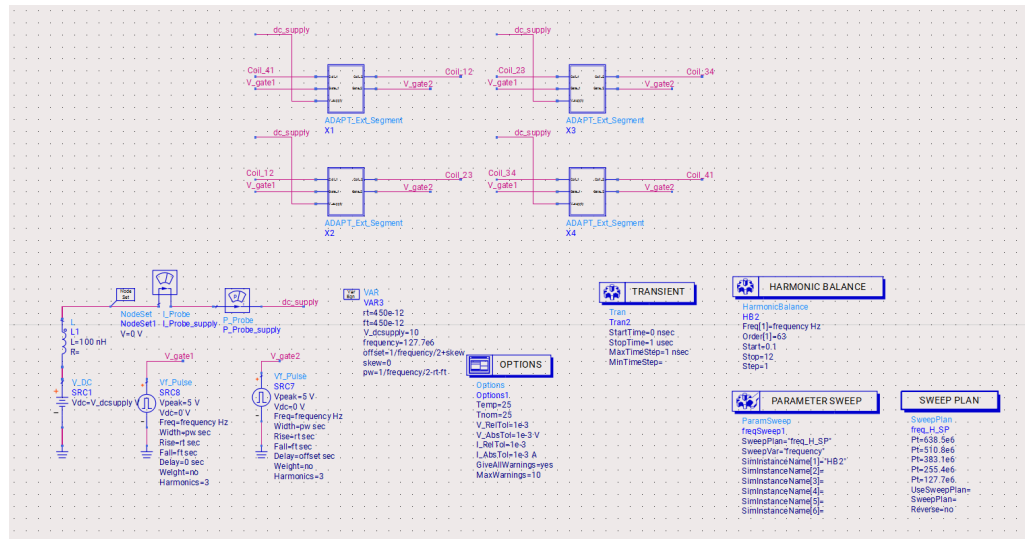


Figure 4.9: ADAPT module coil model used to obtain simulations results.

Following the change of maximum voltage rating of a switch (EPC 2221)  $V_{DC}$  supply voltage for each frequency was adjusted accordingly. Adjusted configurations are presented in table 4.2.

Parameter	Unit	$^1H$	$^{13}C$	$^{15}N$
$L_{seg}$	nH	10	10	10
$R_{seg}$	$\Omega$	0	0	0
$L_{source}$	nH	100	100	100
$R_{source}$	$\Omega$	0	0	0
$f$	MHz	127.7	32.1	12.95
$t_r$	ns	0.45	0.45	0.45
$t_f$	ns	0.45	0.45	0.45
$skew$	ns	0	0	0
$V_{DC,max}$	V	12	4	1.6

Table 4.2: Adjusted  $^1H$ ,  $^{13}C$ , and  $^{15}N$  configurations

### 4.3.2 Circuit simulations results

Again the theoretical magnetic field at each frequency was calculated using equation 1.3 for:

- $\mu_0 = 4\pi \cdot 10^{-7} \frac{N}{A^2}$
- $a = 4.5 \cdot 10^{-2} m$  - ADAPT coil radius
- $z = 19.6 \cdot 10^{-3} m$  - Distance from the coil center at which actual measurement was performed in fabricated ADAPT coil

## $^1H$ simulation results

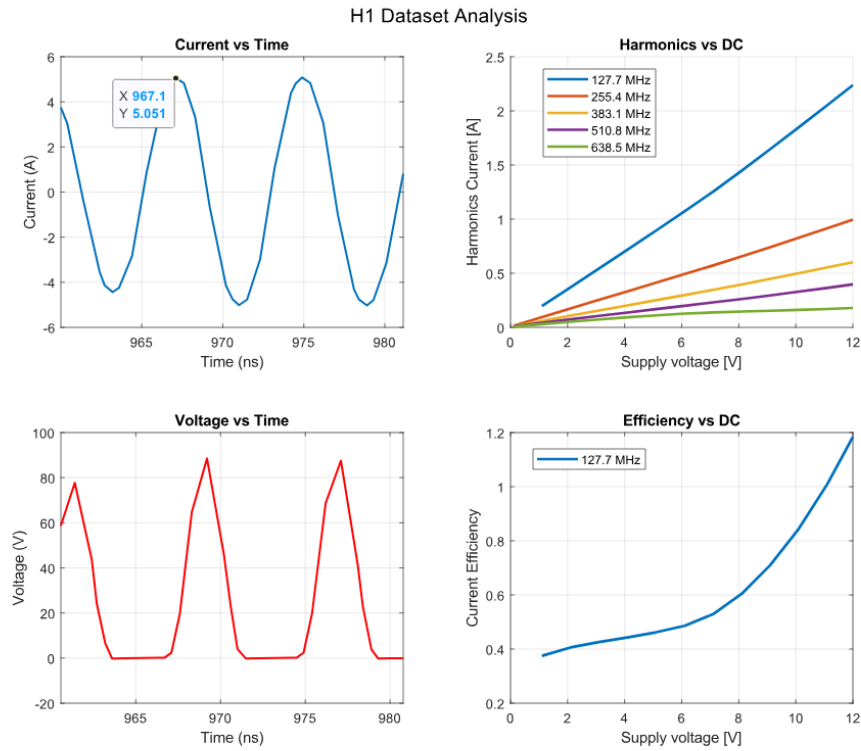


Figure 4.10:  $^1H$  ADAPT module simulation results

Calculated magnetic field at 19.6 mm away from the coil center:

$$B_z = \frac{\mu_0 I a^2}{2(a^2 + z^2)^{3/2}} = 53.8 \mu T \quad (4.7)$$

for:

- $I \approx 5 A$

## $^{13}C$ simulation results

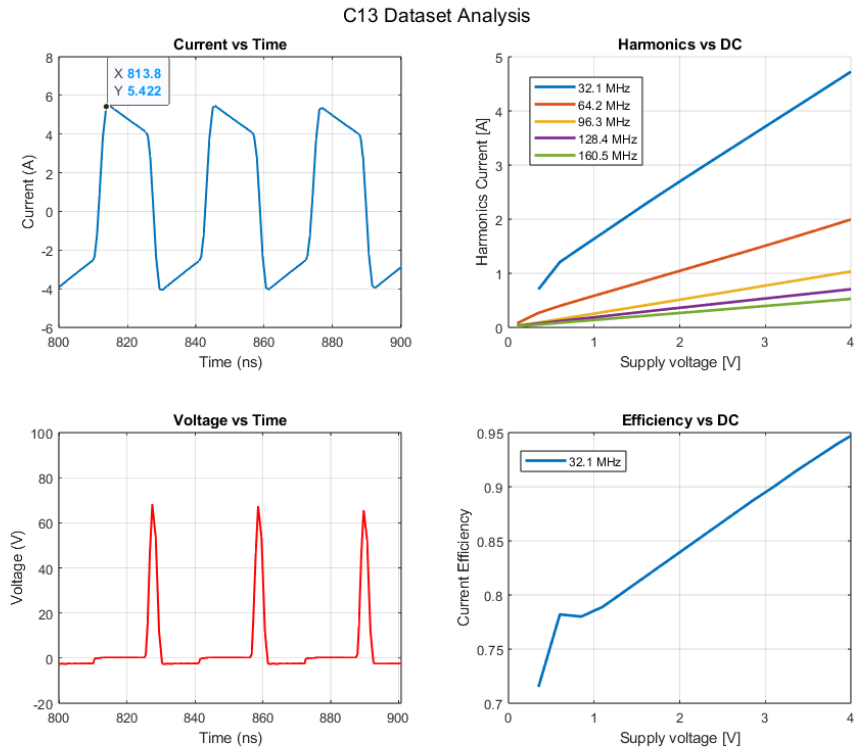


Figure 4.11:  $^{13}C$  ADAPT module simulation results

Calculated magnetic field at 19.6 mm away from the coil center:

$$B_z = \frac{\mu_0 I a^2}{2(a^2 + z^2)^{3/2}} = 54.9 \mu T \quad (4.8)$$

for:

- $I \approx 5.1 A$

## $^{15}\text{N}$ simulation results

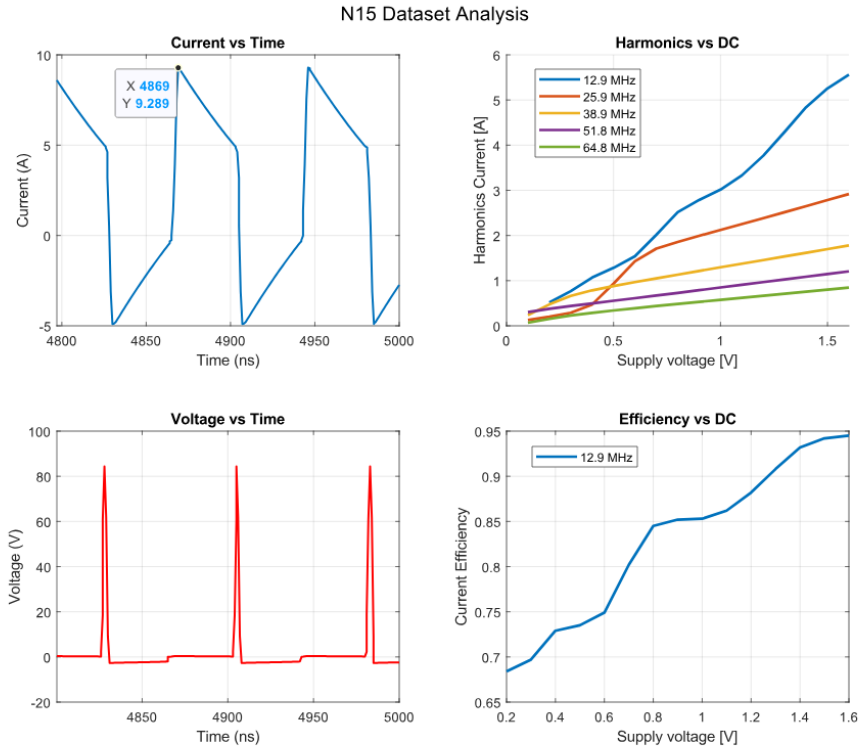


Figure 4.12:  $^{15}\text{N}$  ADAPT module simulation results

Calculated magnetic field at 19.6 mm away from the coil center:

$$B_z = \frac{\mu_0 I a^2}{2(a^2 + z^2)^{3/2}} = 100.1 \mu\text{T} \quad (4.9)$$

for:

- $I \approx 9.3 \text{ A}$

### 4.3.3 ADAPT module magnetic field

Comparing the theoretical values calculated to the reference values gives the expected result of increased magnetic field at each investigated frequency due to increased current in each segment of a coil. The comparison is presented in the table 4.3 below.

Nucleus	Ref. $B_z (\mu\text{T})$	Ref. $I (\text{A})$	ADAPT module $B_z (\mu\text{T})$	ADAPT module $I (\text{A})$
$^1\text{H}$	18.83	1.75	53.8	5.0
$^{13}\text{C}$	36.6	3.4	54.9	5.1
$^{15}\text{N}$	36.6	3.4	100.1	9.3

Table 4.3: Comparison of reference and ADAPT module magnetic field estimations

When the voltage limit was raised so did the resulting currents. This itself creates a new set of criteria related to current handling in a PCB layout, further described in chapter 5.

#### 4.3.4 Gate drive current

Assuming the same rise and fall times at each frequency the gate drive current has a common value across whole frequency range. The gate drive current for EPC 2221 with  $Q_G = 0.85 \text{ nC}$   $t_r/t_f = 0.45 \text{ ns}$  peaks at value  $I_{gate} = 1.4 \text{ A}$ .

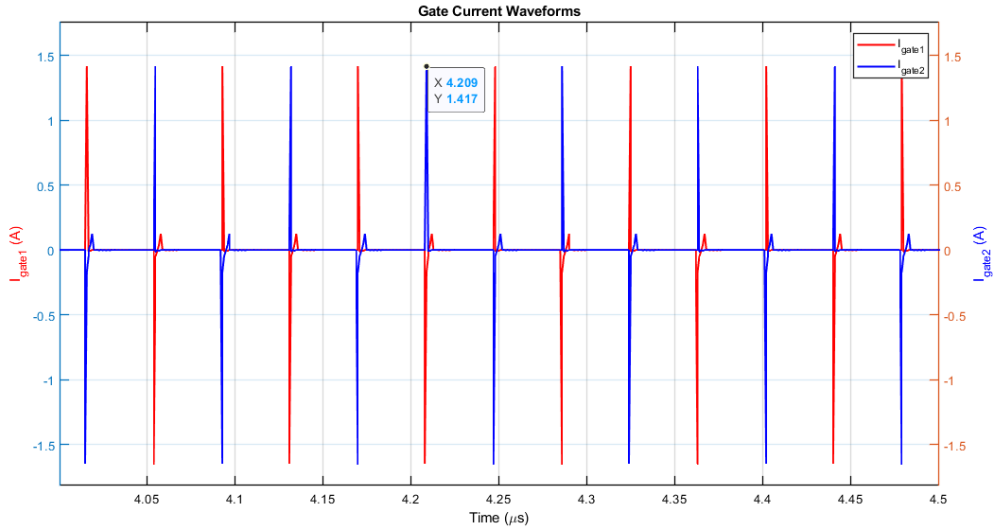


Figure 4.13: Gates drive current

This leaves big margin for implementing FETs with higher gate charge, which usually translates to higher voltage and current ratings. One can estimate the maximum gate charge that TPM2025 can drive with reorganized equation 3.3.

$$Q_{G,max} = I \cdot t = 5 \text{ A} \cdot 0.45 \text{ ns} = 2.25 \text{ nC} \quad (4.10)$$

or in TPM2025 parallel mode:

$$Q_{G,max} = I \cdot t = 7 \text{ A} \cdot 0.45 \text{ ns} = 3.15 \text{ nC} \quad (4.11)$$

# 5 ADAPT module layout

To accommodate the changes required for ADAPT module a new PCB layout had to be created. As described in previous chapters 2 - 4, there are few key changes that enables driving coil at higher power and generating stronger RF magnetic field, like:

1. Coil segments placed on a separate PCB - coil is an assembly of modules
2. Redesigned PCB traces acting as a coil segments with adjusted current rating
3. EPC 21601 replaced with EPC 2221 and TPM2025 driver
4. SN65LVDS117DGG LVDS repeater replaced with 2 SN65EPT21DGKR LVDS to TTL receivers
5. SS-60000-008 socket was replaced with 691321100008 8-pin terminal connector

## 5.0.1 ADAPT module schematic

Schematic of ADAPT module with applied changes is attached in appendix A.

## 5.1 ADAPT module layout overview

To enable making the coil of almost any size or shape the segments are put on a separate PCBs with the complete drive circuit, approach similar to system on module [27] (SoM) common in modern hardware engineering. This allows to make arbitrary connections, achieving even full body sized coil with little to no performance decrease. On the other hand, this shifts the responsibility of ensuring the proper power delivery as well as control signals to assembly design phase. The user of the ADAPT module has to carefully plan the power delivery as well as a proper signal connections to each segment separately.

### Segment inductance estimation

The inductance of the segment is determined by the inductance of a PCB trace as the segment component. Estimation of the trace inductance is done using equations for a micro-strip inductance [28].

$$L = 0.2 \cdot h \cdot l \left( \ln\left(\frac{4h}{w}\right) + 1 \right) [nH] \quad (5.1)$$

Then, for:

$$l = 30 \cdot 10^{-3} m \text{ - length of the trace}$$

$$w = 6 \cdot 10^{-3} m \text{ - width of the trace}$$

$$h = 70 \cdot 10^{-6} m \text{ - thickness of the trace (2oz copper layer)}$$

the inductance is:

$$L = 10.2nH \quad (5.2)$$

Using this estimation final layout was created presented on figure 5.1 below.

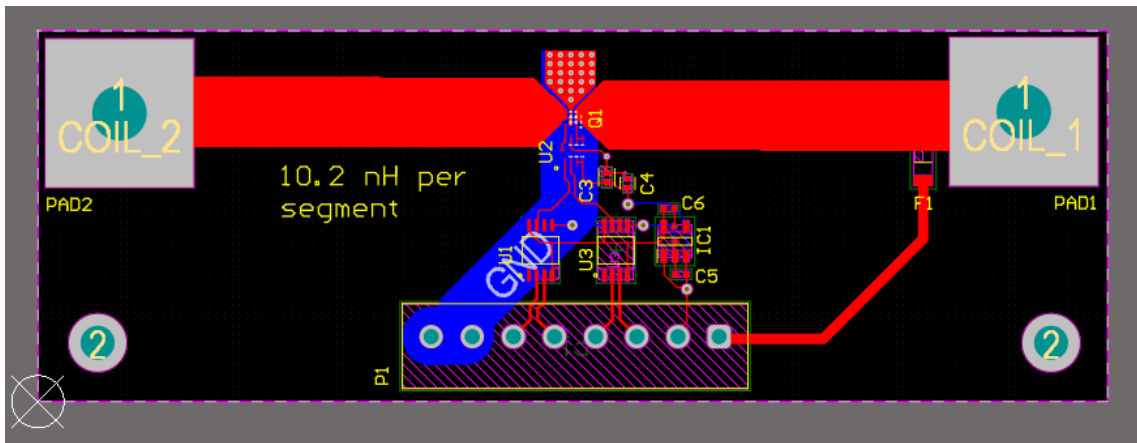


Figure 5.1: ADAPT module PCB layout

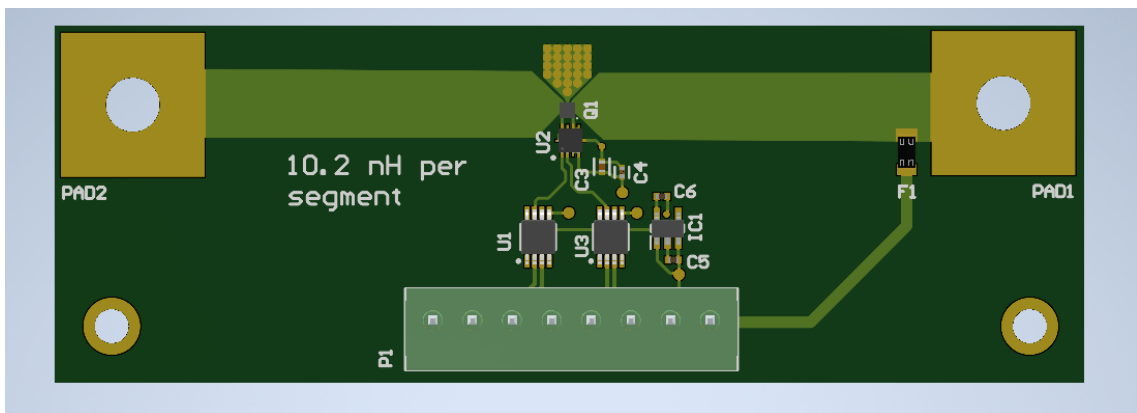


Figure 5.2: ADAPT module PCB visualization

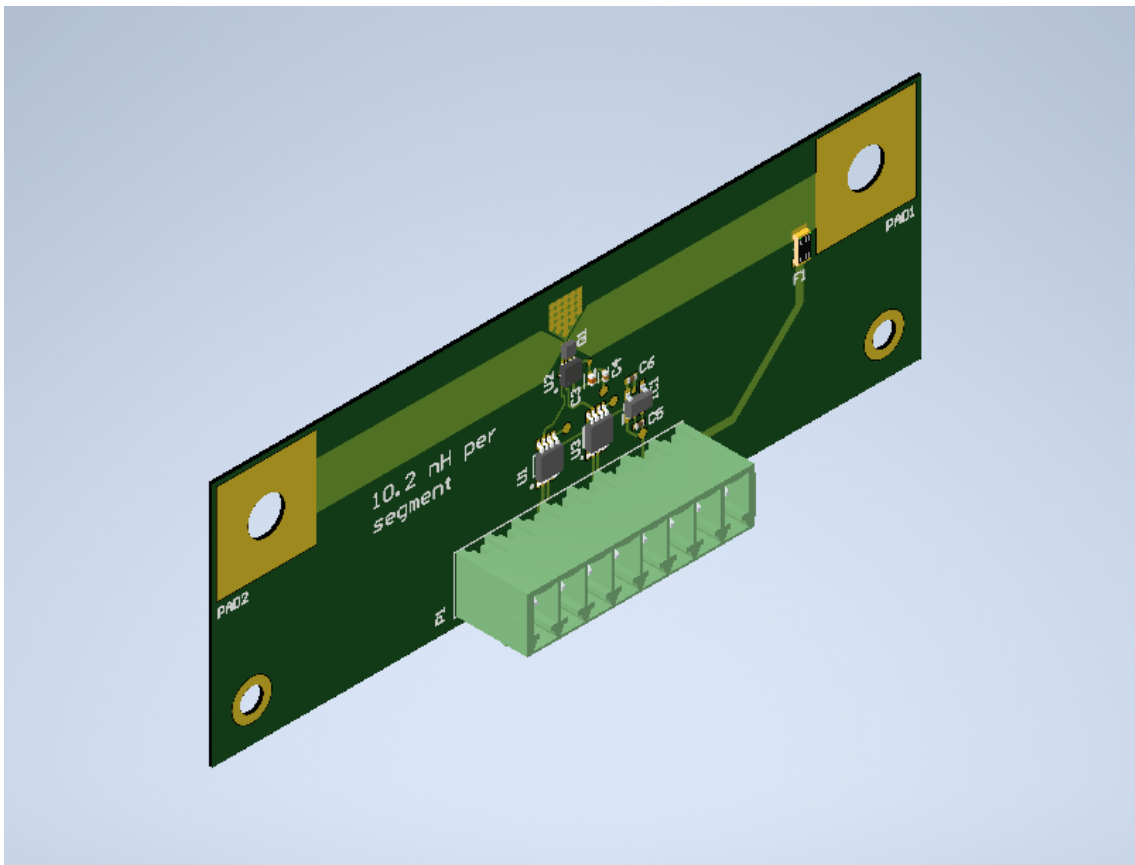


Figure 5.3: ADAPT module PCB side view

### 5.1.1 EPC 2221 with TPM2025

EPC 2221 comes in 9-pin 1.35mm x 1.35mm die. Footprint and 3D model are provided by the manufacturer at the device website [5]. EPC 2221 characteristics were described in the table 3.3 in section 3.6.1.

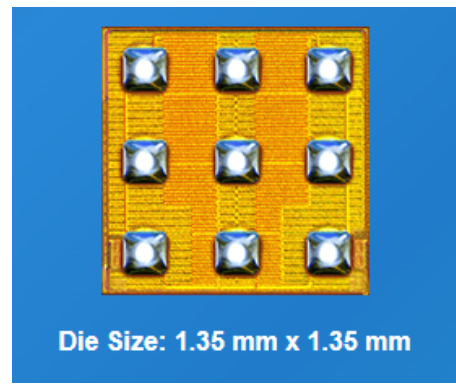


Figure 5.4: EPC 2221 die.

Source: *EPC2221: 100V Enhancement Mode GaN Transistor* [5]

TPM2025 is manufactured in standardized QFN2X2-10 package. The characteristics of the device are presented in the table 3.5 in section 3.6.1.

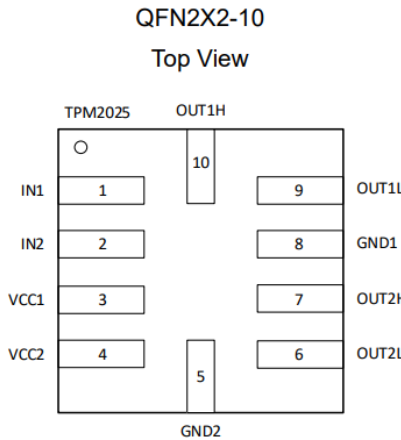


Figure 5.5: TPM2025 pinout.

Source: *TPM2025 / TPM2025Q Automotive Dual-Channel Ultra-Highspeed GaN Predriver | Figure 14 [25]*

### 5.1.2 SN65EPT21DGKR LVDS to TTL repeater

Modularity of the ADAPT module is achieved using small, single input and output LVDS to TTL repeater SN65EPT21DGKR IC. On a single module 2 of such ICs have to be used to drive segments independently. Use of the LVDS to TTL repeater allows control to be a pair of differential signals, significantly reducing the noise of a low voltage control signal supplied to the module. Next, the differential signal is translated on the PCB to the ground referenced TTL logic level, which allows to use it with a TPM2025. Major advantage of this approach is that the ground referenced TTL signal is less prone to noise in high EMI environment.

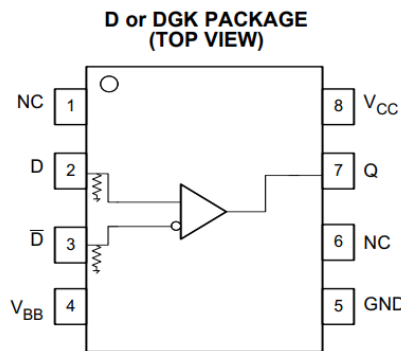


Figure 5.6: SN65EPT21DGKR pinout.

Source: *SN65ELT21 5-V PECL-to-TTL Translator [29]*

### 5.1.3 8-pin terminal connector

Driving higher current requires the connector rated appropriately. Regular ethernet socket is rated only up to 1.5 A. Terminal connector like 691321100008 is rated up to 10 A of current per pin for a continuous operation, therefore it's suitable to drive ADAPT module.

## 5.2 Estimated cost of the ADAPT module

The total cost per complete PCB assembly is estimated based on the DigiKey electronics part supplier if not otherwise stated. The example cost of PCB manufacturing was estimated using JLCPCB online tools.

Name	Quantity	Total Cost
C1005X5R1E474K050BB (Capacitor)	1	0.1\$
C0402C104K8PACTU (Capacitor)	1	0.1\$
GRM155R61A475KEAAD (Capacitor)	2	0.04\$ <sup>1</sup>
3413.0328.22 (Fuse)	1	0.52\$
ADP151AUJZ-3.3-R7 (LDO)	1	2.24\$
691321100008 (Terminal Connector)	1	1.32\$
EPC2221 (FET)	1	3.55\$
SN65EPT21DGKR (LVDS to TTL Receiver IC)	2	8.58\$
TPM2025Q-FC1R-S (Gate Driver IC)	1	2.46\$
PCB (min. quantity: 5pcs; price incl. shipping)	1	≈ 3\$ per PCB <sup>2</sup>
<b>Sum</b>		21.91\$

Table 5.1: Cost estimation of ADAPT module



# 6 ADAPT module - assembly example

So far the work done was focused on improvement of the single module that hold 2 consecutive segments. To work as a RF coil, few of presented modules must be connected together in circular pattern. It is done by connecting 2 PCB, one on the top of the other. The connections must be made alternately and the minimal number of segments is 4 due to direct connection of PCBs.

## 6.1 9 cm diameter coil

A 9 cm diameter coil is proposed, to compare the coil performance with respect to reference ADAPT design from [1]. Based on the cost per segment estimation done in table 5.1, the total cost of the 9 cm coil made using ADAPT modules is  $\approx 87.64\$$ . There is a significant decrease in cost, compared to reference design estimation presented in Table 1 in “Any-nucleus distributed active programmable transmit coil”, where the total cost was  $115.84\$$ . 9 cm coil is presented on figures 6.1 and 6.2 below.

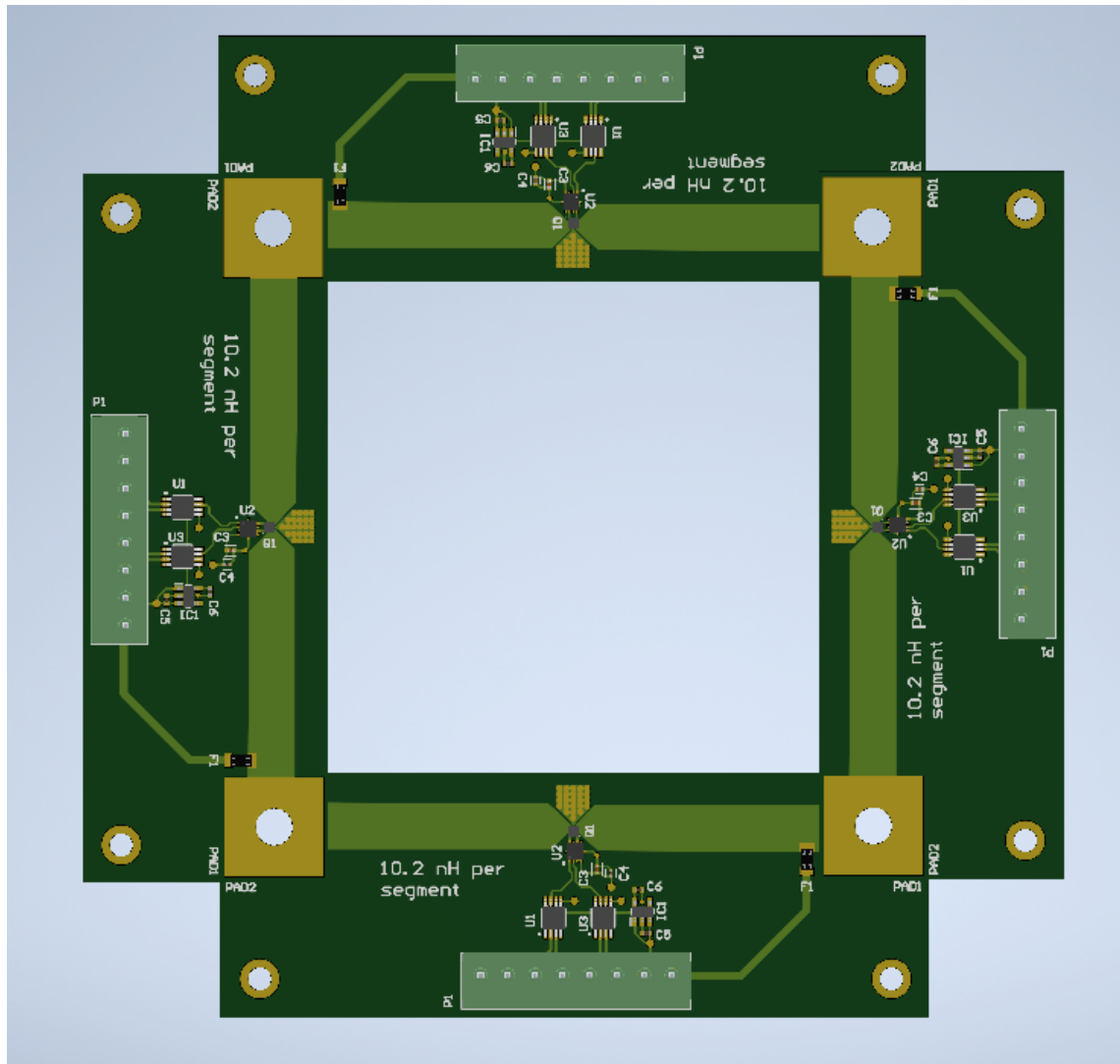


Figure 6.1: ADAPT 9cm coil created using ADAPT modules. Diameter is equal to  $d = 9\text{ cm}$

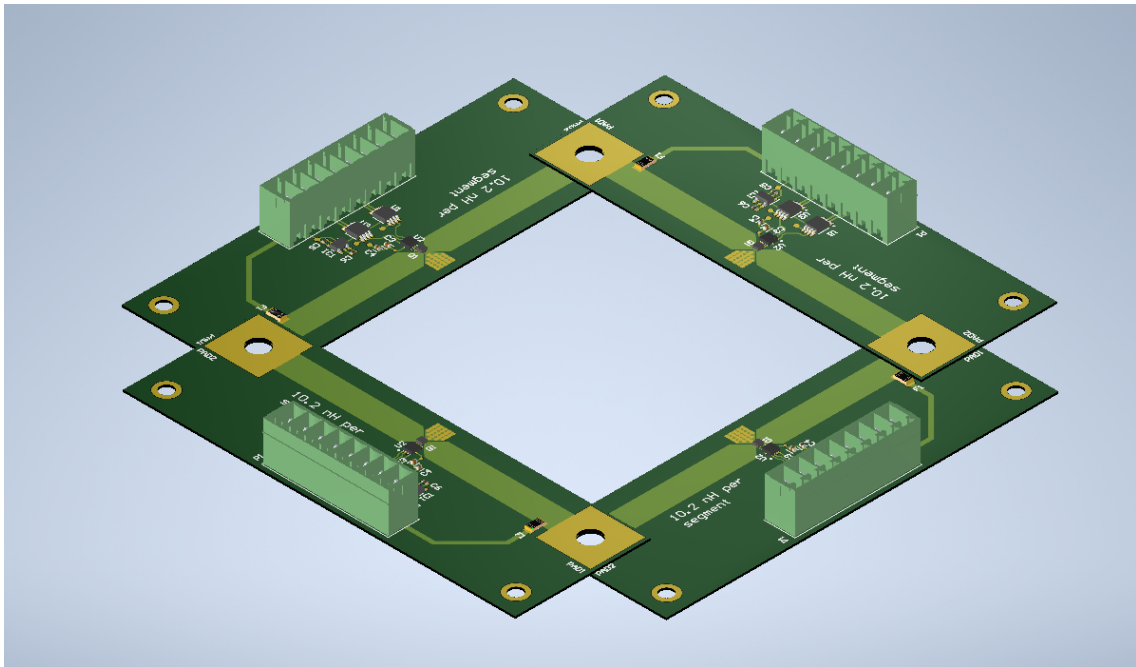


Figure 6.2: ADAPT modular coil side view with PCBs stacked

## 6.2 Full body coil

The main advantage of modular approach to ADAPT coil design is it's scalability. Using ADAPT modules it is possible to extend the coil to almost any size without sacrificing the performance. On figures 6.3 and 6.4 presented is 60cm diameter coil, where the diameter is the typical bore diameter of the MRI, therefore creating the physical constraint for the RF coil size. The coil is made with 20 ADAPT modules connected in circular pattern. Cost estimation is done based on estimation done in chapter 5 in table 5.1. Total cost of manufacturing the full body coil using ADAPT modules is  $\approx 438.2\$$ . Full body coil assembly is presented on figures 6.3 and 6.4 below.

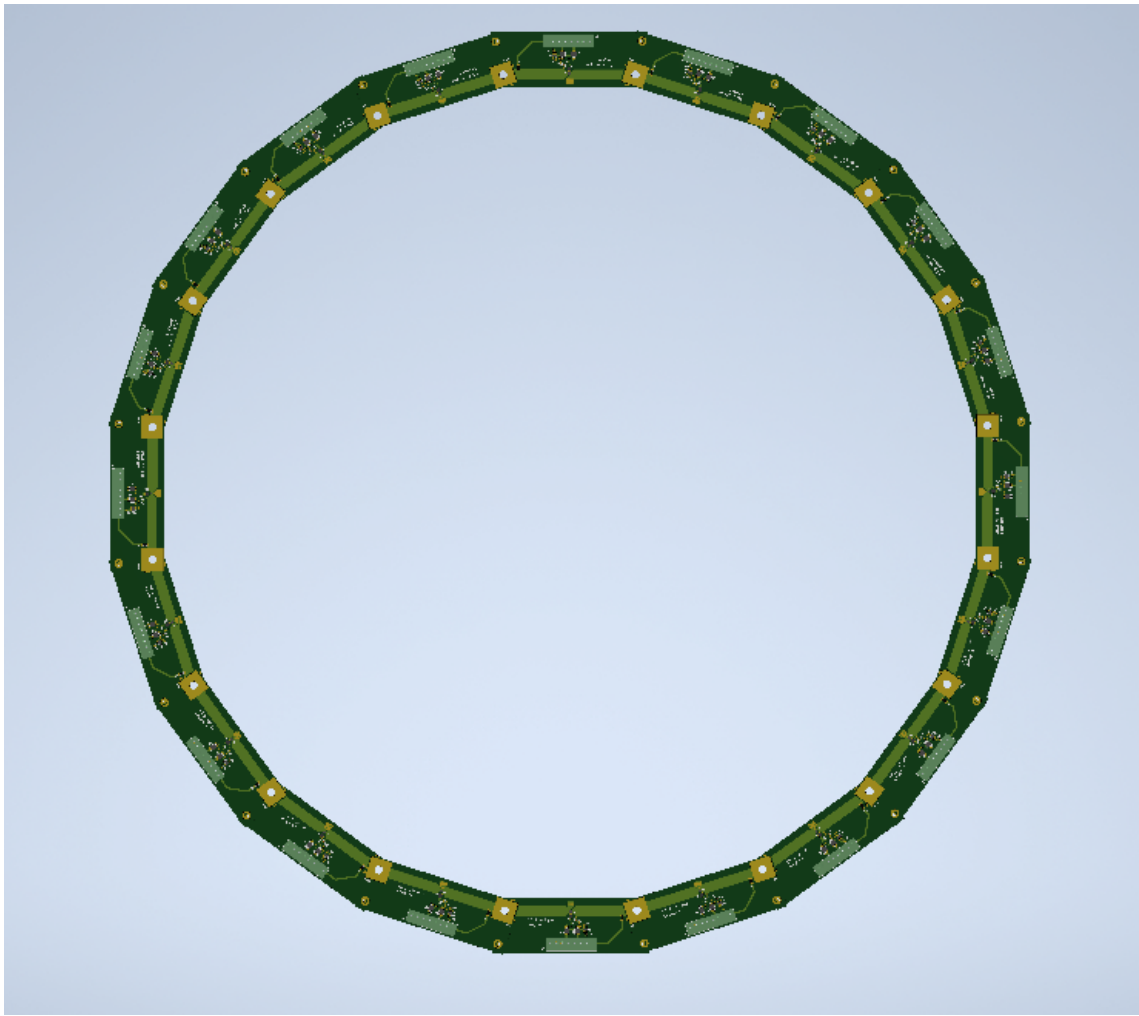


Figure 6.3: ADAPT full body coil created using ADAPT modules. Diameter is equal to  $d = 60\text{ cm}$



Figure 6.4: ADAPT modular full body coil with visible alternating connections of PCBs

## 7 Summary and conclusions

The ADAPT module presented in this paper extends the limits of reference ADAPT design. One of the primary advantages of it is the scalability. It can be freely extended in 2D space using direct PCB connections with examples presented in chapter 6, or it could create a 3D coil structures using flat braided wire strips (flexible copper cables) at cost of increased inductance, which is not easily done with regular FR-4 PCBs. The solution to this for both reference and modular design might be use of a flexible PCB, this however would require a completely new investigation and redesign.

Additionally, ADAPT module offers significant advantage in 2D space, as increasing the size of the coil requires simply more modules added into the structure that creates the coil loop, whereas in reference design, increasing the size of the coil requires redesign of a PCB. What's more, this leads to the increased robustness and easier maintenance of the coil, even though if rare, in such a situation it could only require to replace single module, instead of a whole coil, meaning that the operational downtime of the MRI could be minimized.

Modular approach brings down the cost of the coil. Minimal working example of 9 cm in diameter coil costs as little as  $\approx 88 \text{ USD}$ . This can be decreased even further with bulk parts ordering and finding even cheaper parts alternatives.

Currently the primary limit of the ADAPT module is the FET driver. Market research showed that there is very limited number of FET drivers that can operate at high speed switching FET with high power ratings. Even in this paper it was considered that any of current voltage or current limits can be easily dealt with by selecting FETs like GS66516B discussed in section 3.6.1, but it cannot be easily driven at high speed due to extreme peak gate current. If use of GS66516B was possible, the RF magnetic field generated as high as:

$$I = \frac{V \cdot t}{L} = \frac{650 \text{ V} \cdot 0.45 \text{ ns}}{10 \text{ nH}} = 29.3 \text{ A} \quad (7.1)$$

resulting in magnetic field:

$$B_1 = \frac{\mu_0 I a^2}{2(a^2 + z^2)^{3/2}} = 0.32 \text{ mT} \quad (7.2)$$

This is assuming conditions similar to the ADAPT module coil:

$$L = 10 \text{ nH}$$

$$B_0 = 3 \text{ T}$$

$$f_{max} = 127.7 \text{ MHz}$$

$$t_r/t_f = 0.45 \text{ ns}$$

$$\mu_0 = 4\pi \cdot 10^{-7} \frac{\text{N}}{\text{A}^2}$$

$$a = 4.5 \cdot 10^{-2} \text{ m} - \text{ADAPT coil radius}$$

$$z = 19.6 \cdot 10^{-3} \text{ m}$$

However, this is only a theoretical value accounting for a single FET. With modular approach the current rating of up to 10 A is measured per module, which means the total

current of the coil and resulting magnetic field could not be matched even with conventional RF coils. Considering full body coil described in chapter 6, assuming use of an ideal switch and driving the segments at the connector limit of 10 A we get resulting in magnetic field:

$$B_1 = \frac{\mu_0 \cdot I \cdot N \cdot a^2}{2(a^2 + z^2)^{3/2}} = 0.42 \text{ mT} \quad (7.3)$$

for:

$I = 10 \text{ A}$  - current per segment

$N = 20$  - modules count

$\mu_0 = 4\pi \cdot 10^{-7} \frac{N}{A^2}$

$a = 30 \cdot 10^{-2} \text{ m}$  - coil radius

$z = 19.6 \cdot 10^{-3} \text{ m}$

## 7.1 Summary

This paper presents the investigation of the performance improvements in ultra-wide band magnetic field coil by addressing key limitations of the solution provided by Han et al. in “Any-nucleus distributed active programmable transmit coil”. By introduction of modular architecture, achieved was a significant advancement over the reference ADAPT coil design throughout a multi-nuclear frequency range.

The modular design approach implemented extends the coil scalability, enabling arbitrary coil size without performance degradation. The layout was optimized and traces calculated for  $\approx 10 \text{ nH}$  which allows to driver the coil with high current, simulated to achieve almost 10 A at  $^{15}\text{N}$  larmor frequency.

Performance analysis demonstrates significant improvements across multiple nuclei frequencies, with 185% magnetic field increase at  $^1\text{H}$ , 50% at  $^{13}\text{C}$  and 173% at  $^{15}\text{N}$ . This should give substantial increase in imaging resolution and clarity in multinuclear MRI.

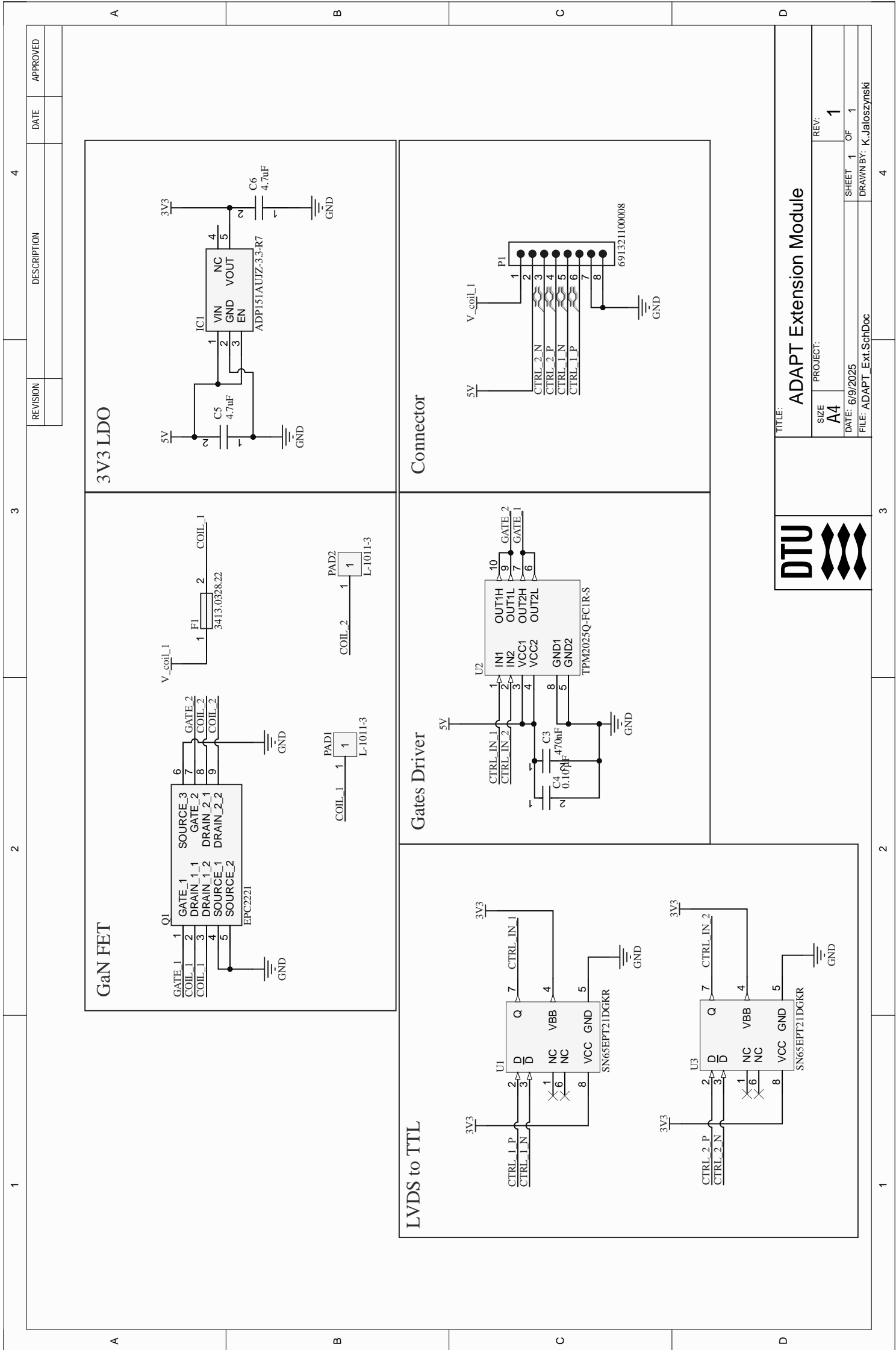
The research gives a basis for ultra wide band field generation in MRI applications, expanding the diagnostic capabilities with X-nuclei imaging techniques that were unavailable due to technical limitations.

# Bibliography

- [1] Victor Han et al. "Any-nucleus distributed active programmable transmit coil". In: *Magnetic Resonance in Medicine* 92 (2024), pp. 389–405.
- [2] A. Ruh and V. G. Kiselev. "Calculation of Larmor precession frequency in magnetically heterogeneous media". In: *Concepts in Magnetic Resonance Part A* 48A.2 (2019).
- [3] James C. Simpson et al. *Simple Analytic Expressions for the Magnetic Field of a Circular Current Loop*. Technical Memorandum NASA/TM-2013-217919. Kennedy Space Center, Florida: NASA, 2013.
- [4] Ruomin Hu et al. "X-nuclei imaging: Current state, technical challenges, and future directions". In: *Journal of Magnetic Resonance Imaging* 52.1 (2020), pp. 335–350.
- [5] *EPC2221: 100V Enhancement Mode GaN Transistor*. Efficient Power Conversion Corporation. 2022. URL: <https://epc-co.com/epc/products/gan-fets-and-ics/epc2221>.
- [6] *EPC21601 – eToFTM Laser Driver IC Datasheet*. Efficient Power Conversion Corporation (EPC). 2023. URL: [https://epc-co.com/epc/Portals/0/epc/documents/datasheets/EPC21601\\_datasheet.pdf](https://epc-co.com/epc/Portals/0/epc/documents/datasheets/EPC21601_datasheet.pdf).
- [7] Texas Instruments. *SN65LVDS117 Dual 8-Port LVDS Repeater Datasheet (Rev. F)*. Rev. F, SLLS369F. Texas Instruments Incorporated. Feb. 2005. URL: <https://www.ti.com/lit/gpn/SN65LVDS109>.
- [8] Stewart Connector. *Jack, Vertical, FTP, Cat6 - SS-60000-008*. Farnell Product Page. Available: <http://uk.farnell.com/stewart-connector/ss-60000-008/jack-vertical-ftp-cat6/dp/1572187>. Accessed: 2025. URL: <http://uk.farnell.com/stewart-connector/ss-60000-008/jack-vertical-ftp-cat6/dp/1572187>.
- [9] Inc. Freescale Semiconductor. *Field Effect Transistors in Theory and Practice*. Originally published 1993, revised 2009. 2009. URL: <https://www.nxp.com/docs/en/application-note/AN211A.pdf>.
- [10] International Journal of Novel Research and Development. *A Review Study on Fundamentals of HEMT Device and Technology*. Online. HEMT is discussed as a specialized field-effect transistor. Accessed: 2025. URL: <https://www.ijnrdr.org/>.
- [11] Z. Yin et al. "Enhanced transport in transistor by tuning transition-metal oxide electronic states interfaced with diamond". In: *Science Advances* 4 (2018).
- [12] Author Unknown. "Limitations of the intrinsic cut-off frequency to correctly quantify the speed of nanoscale transistors". In: *arXiv preprint arXiv:1611.03856* (2016). Accessed: 2025-06-06. URL: <https://arxiv.org/pdf/1611.03856.pdf>.
- [13] Diamond Materials GmbH. *Thermal Properties of CVD Diamond*. Accessed: 2025-06-07. Summarizes thermal conductivity (>1800 W/mK at 300K) and other key properties of CVD diamond. 2025. URL: <https://www.diamond-materials.com/en/cvd-diamond/thermal/>.
- [14] Hiroshi Amano, Hideki Sawaki, and Isamu Akasaki. "High Thermal Conductivity of Gallium Nitride (GaN) Crystals Grown by HVPE Process". In: *Materials Transactions* 48.10 (2007), pp. 2782–2786. DOI: 10.2320/matertrans.MRP2007109. URL: [https://www.jstage.jst.go.jp/article/matertrans/48/10/48\\_MRP2007109/\\_article](https://www.jstage.jst.go.jp/article/matertrans/48/10/48_MRP2007109/_article).
- [15] F. Zhao et al. "A Review of Diamond Materials and Applications in Power Semiconductor Devices". In: *Materials* 17 (2024). Academic Editor: Antonio Polimeni. Received: 20 June 2024; Revised: 6 July 2024; Accepted: 8 July 2024; Published:

- 11 July 2024., p. 3437. DOI: 10.3390/ma17143437. URL: <https://pmc.ncbi.nlm.nih.gov/articles/PMC11278176/pdf/materials-17-03437.pdf>.
- [16] Masoud Beheshti. *Wide-bandgap semiconductors: Performance and benefits of GaN versus SiC*. 2020. URL: <https://www.ti.com/lit/an/slyt801/slyt801.pdf>.
- [17] Jelena Loncarski, Hussain A. Hussain, and Alberto Bellini. “Efficiency, Cost, and Volume Comparison of SiC-Based and IGBT-Based Full-Scale Converter in PMSG Wind Turbine”. In: *Electronics* 12.2 (2023), p. 385.
- [18] David Reusch and Johan Strydom. *Improving Performance of High Speed GaN Transistors Operating in Parallel for High Current Applications*. Presentation. 2016. URL: [https://epc-co.com/epc/Portals/0/epc/documents/presentations/EPC\\_Paralleling\\_High\\_Speed\\_GAN\\_Reusch.pdf](https://epc-co.com/epc/Portals/0/epc/documents/presentations/EPC_Paralleling_High_Speed_GAN_Reusch.pdf).
- [19] Maximilian Nitzsche et al. “Comprehensive Comparison of a SiC MOSFET and Si IGBT Based Inverter”. In: *IEEE Transactions on Power Electronics* (2021). Example journal; please update with actual journal if available.
- [20] Maurizio Di Paolo Emilio. *A Unified View and Price-Performance Analysis of IGBTs & GaN, SiC, and Silicon FETs*. 2023. URL: <https://www.powerelectronicsnews.com/a-unified-view-and-price-performance-analysis-of-igbts-gan-sic-and-silicon-fets/>.
- [21] Nexperia. *MOSFET & GaN FET Application Handbook*. 2020. URL: [https://assets.nexperia.com/documents/user-manual/Nexperia\\_document\\_book\\_MOSFETGaNFETApplicationHandbook\\_2020.pdf](https://assets.nexperia.com/documents/user-manual/Nexperia_document_book_MOSFETGaNFETApplicationHandbook_2020.pdf).
- [22] Nicholas Oborny and Ashish Ojha. *Understanding Smart Gate Drive*. Tech. rep. SLVA714D. Application Report, revised March 2021. Texas Instruments, 2021. URL: <https://www.ti.com/lit/an/slva714d/slva714d.pdf>.
- [23] Jan Zawilak and Maciej Gwoździewicz. “Start-up of large power electric motors with high load torque”. In: *Przegląd Elektrotechniczny* 95.6 (2019).
- [24] Yong Xie and Paul Brohlin. *Optimizing GaN performance with an integrated driver*. Application Report. Texas Instruments, 2016.
- [25] 3PEAK Incorporated. *TPM2025 / TPM2025Q Automotive Dual-Channel Ultra-Highspeed GaN Predriver*. <https://static.3peak.com/res/doc/ds/Datasheet TPM2025 - TPM2025Q.pdf>. Rev. A.2, July 10, 2023. 2023.
- [26] Efficient Power Conversion Corporation. *EPC21601: 40 V, 15 A, 3.3 V Logic, eToF™ Laser Driver IC*. Accessed: 2025-06-08. 2025. URL: <https://epc-co.com/epc/products/gan-fets-and-ics/epc21601>.
- [27] AMD. *What is a SOM*. <https://www.amd.com/en/products/system-on-modules/what-is-a-som.html>. Accessed: 2025-06-10. 2025.
- [28] *Design Guide for High-Speed Controlled Impedance Circuit Boards*. IPC-2141A Standard. Section on microstrip inductance formulas. 1996.
- [29] Texas Instruments. *SN65ELT21 5-V PECL-to-TTL Translator*. Tech. rep. SLLS923. Texas Instruments, June 2009. URL: <https://www.ti.com/lit/ds/symlink/sn65elt21.pdf?ts=1749533761484>.

## A ADAPT extension module schematic



# List of Acronyms

<b>ADAPT</b>	Any-nucleus Distributed Active Programmable Transmit (coil)
$B_0$	Primary static magnetic field
$B_1$	Oscillating (RF) magnetic field
<b>CEA</b>	Commissariat à l'énergie atomique et aux énergies alternatives (French Alternative Energies and Atomic Energy Commission)
<b>EMI</b>	Electromagnetic Interference
<b>FET</b>	Field Effect Transistor
<b>GaN</b>	Gallium Nitride
<b>HEMT</b>	High Electron Mobility Transistor
<b>IC</b>	Integrated Circuit
<b>IGBT</b>	Insulated Gate Bipolar Transistor
<b>LC</b>	Inductor-Capacitor oscillator
<b>LDO</b>	Low Dropout Regulator
<b>LVDS</b>	Low Voltage Differential Signaling
<b>MRI</b>	Magnetic Resonance Imaging
<b>MOSFET</b>	Metal Oxide Semiconductor Field Effect Transistor
<b>PCB</b>	Printed Circuit Board
<b>RF</b>	Radio Frequency
<b>RDS(on)</b>	On-state Resistance (of FET)
<b>SiC</b>	Silicon Carbide
<b>SoM</b>	System on Module
<b>TMO</b>	Transition Metal Oxide
<b>TMOD</b>	Transition Metal Oxide interfaced with Diamond (FET)
<b>TTL</b>	Transistor-Transistor Logic
<b>VDS</b>	Drain-Source Voltage
<b>VGS</b>	Gate-Source Voltage
<b>VD</b>	Drain Voltage
<b>ID</b>	Drain Current
<b>QG</b>	Gate Charge
<b>tr/tf</b>	Rise/Fall Time
<b>VDC</b>	Direct Current Voltage

**GHz** Gigahertz

**MHz** Megahertz

**nH** Nanohenry

**pF** Picofarad

**mT** Millitesla

**µT** Microtesla



Technical  
University of  
Denmark

Elektrovej, Building 327  
2800 Kgs. Lyngby  
Tlf. 4525 1700

[www.space.dtu.dk](http://www.space.dtu.dk)